This is to certify that the

thesis entitled

Magnetothermal Oscillations in

Graphite Intercalation Compounds

presented by

James Eadus Huffman

has been accepted towards fulfillment
of the requirements for

Ph.D. degree in Physics

J. S. Kovacs

Major professor

Date June 7, 1983

MAGNETOTHERMAL OSCILLATIONS IN GRAPHITE INTERCALATION COMPOUNDS

By

James Eadus Huffman

A DISSERTATION

Submitted to
Michigan State University
in partial fulfillment of the requirements
for the degree of

DOCTOR OF PHILOSOPHY

Department of Physics and Astronomy

1983

ABSTRACT

MAGNETOTHERMAL OSCILLATIONS IN
GRAPHITE INTERCALATION COMPOUNDS

by

James Eadus Huffman

The Fermi surface (FS) of $SbCl_5$-GIC's for stage 1 to stage 8 has been studied using the magnetothermal oscillation method. The majority of the measurements were performed at about 1K and in magnetic fields up to 5T (50kG). Frequencies of the dHvA oscillations were determined by a fast Fourier transform analysis of the raw data, using an on-line computer. The results show a monotonic increase in the area of the FS with decreasing stage index and a weak monotonic increase of the charge transfer coefficient, f, with increasing stage index. The shape of the FS, as deduced from the angle dependence of the frequencies, is consistent with a cylindrical surface or an elongated ellipsoidal one. For the stage 6 sample we have also determined the effective mass of the carriers in the plane perpendicular to the c-axis, and find that $m^* = 0.3\ m_o$, in agreement with calculated masses based on the Slonczewski-Weiss-McClure (SWMcC) model of the band structure of graphite. Our results are in good agreement with a model for the band structure of GIC's based on the rigid band model (RBM) when zone folding along the c-axis is employed.

DEDICATION

I gratefully dedicate this work to my wife, Ann, and to the rest of my family.

ACKNOWLEDGMENTS

It is a pleasure to acknowledge the guidance and helpful insight of Professor F.J. Blatt. I have also benefited from numerous discussions with Professors S.A. Solin, S.D. Mahanti, and P.A. Schroeder. There are many others, too numerous to list, to whom I owe thanks, but in particular D.L. Edmunds who has been instrumental in setting up the computer interface. Finally, I sincerely thank my typist, S. Lindsay, for her remarkable tolerance, humor, and speed.

The financial support of the National Science Foundation is gratefully acknowledged.

TABLE OF CONTENTS

LIST OF TABLES

LIST OF FIGURES

INTRODUCTION

This dissertation describes a study of the Fermi surface (FS) of a group of graphite intercalation compounds (GIC's) using the magneto-thermal oscillation technique. The subject of GIC's spans many scientific fields. These compounds have been heavily researched in the last few years and considerable progress has been made toward an understanding of the nature of these synthetic, laminar materials. However some topics, one of which being the electronic structure, remain controversial. In recent years conflicting FS data on GIC's has been published. As well, fundamentally different models have been proposed to describe the electronic structure of GIC's. We have made a careful experimental study of the FS for one group of these compounds and have analyzed our results on the basis of two competing theories. We find one of these is in better agreement with our observations.

CHAPTER ONE

DEFINITION AND MEASUREMENT OF THE FERMI SURFACE

1.1 Introduction

In this chapter we will briefly discuss the concept of a Fermi surface and the quantum oscillatory effects used to experimentally determine its geometrical properties.

1.2 The Fermi Surface

A metal could be defined as "a solid with a Fermi surface."[†] Thus, a complete description of the Fermi surface of a solid is essential to an understanding of its electronic (metallic) properties. In this section a brief description of the Fermi surface and its utility is given.

The Fermi surface (FS) is the surface of constant energy in momentum space or 'k-space' within which, at T = OK, all occupied electron energy levels are contained. Hence, the FS is not a surface in real space, but in an abstract, reciprocal space. For a free electron gas, the FS is a sphere whose radius is determined by the number density of electrons. The occupied electronic states are distributed uniformly within the sphere. For a material with a crystalline structure and containing valence or conduction electrons, the shape of the FS is modified due to the periodic lattice potential. The FS is generally shown within the k-space image of the Wigner-Seitz cell of the crystal, i.e. the first Brillioun zone (see references 1 and 2). Given a full description of the FS, properties which depend on the electronic or

[†]A.R. Macintosh.

quasiparticle distribution, such as transport coefficients and equilibrium and optical properties can be calculated.[2]

The Fermi surface for a material can be calculated from a one-electron energy band structure of the system, as in section 4.3, then compared to an experimental measurement of the FS. We now turn to the method by which this surface can be determined experimentally.

1.3 Theory of the Experiment

In section 1.3.1, we present an explanation of the origin of quantum oscillatory effects and conclude the section by giving a formal expression for the oscillatory free energy of a Bloch electron gas, as derived by Lifshitz and Kosevitch.[3] This formal expression is related to a measurable quantity through a thermodynamic analysis in section 1.3.2. The final result of this analysis is discussed in section 1.3.3.

1.3.1 History and Physical Origin of Quantum Oscillations

Quantum oscillatory effects were first observed in 1930 by W. de Haas and P. van Alphen.[4] They discovered oscillations in the magnetic moment of Bismuth as a function of magnetic field intensity. The value of these observations in providing FS data was not fully realized until almost 20 years later when Onsager developed the relation,[5]

$$\Delta \left(\frac{1}{H}\right) = \frac{2\pi e}{\hbar c} \frac{1}{A_{ext}} \qquad 1.1$$

In this equation, $\Delta(\frac{1}{H})$ is the change in 1/H through one complete oscillation, and A_{ext} is the extremal cross sectional area of a segment of the FS perpendicular to the magnetic field direction (see Figure 1.1).

The reciprocal of $\Delta(\frac{1}{H})$ is called the de Haas-van Alphen frequency, and is written as F. This remarkably simple expression holds for all quantum oscillatory effects including, among others, the de Haas-van Alphen effect, magneto-thermal oscillations, and the Shubnikov-de Haas effect. Basically, the only difference between these phenomena is that in each case a different measurable quantity exhibits the dHvA oscillations. For the magneto-thermal oscillations technique (MTO), one detects lattice temperature oscillations; in the Shubnikov-de Haas technique (SdH) one detects oscillatory behavior in the electrical conductivity.

We now give a quasi-classical derivation of Equation 1.1. We begin by assuming that charged particle orbits in a magnetic field are quantized according to the Bohr-Sommerfeld relation,

$$\oint_{\text{orbit}} \vec{P} \cdot d\vec{r} = (n + \gamma)\, 2\pi\hbar \; ; \quad n = \text{integer}, \; \gamma = \text{constant}. \qquad 1.2$$

The total particle momentum, $\vec{P}$, in a magnetic field is given by

$$\vec{P} = \hbar\vec{k} + q\vec{A}/c \; ; \quad \vec{H} = \text{curl } \vec{A}, \; \hbar\vec{k} = \text{kinetic momentum} \qquad 1.3$$

and when used in the above expression gives

$$\oint \vec{P} \cdot \; d\vec{r} = -\frac{2q}{c}\,\Phi + q/c\Phi = -q/c\,\Phi \qquad 1.4$$

where Φ is the magnetic flux enclosed in the real space orbit. Combining Equations 1.2 and 1.4 and substituting (-e) for q,

$$\Phi_n = (n + \gamma)\,\frac{2\pi\hbar c}{e} \qquad 1.5$$

which quantizes the flux through the real space orbits. Real space and reciprocal space (k-space) trajectories are related through a scale

factor, $\delta r/\delta k = \hbar c/eH$, and a rotation of $\pi/2$ so that k-space orbits are also quantized, i.e.,

$$A_n = (n + \gamma)\, 2\pi e/\hbar c\, H \qquad 1.6$$

where A_n is the area in k-space enclosed by the orbit with quantum number n.

Using this we find that consecutive orbits n and n + 1 of equal area are separated by fields given by

$$\Delta\left(\frac{1}{H}\right) = \left(\frac{1}{H_{n+1}} - \frac{1}{H_n}\right) = \frac{2\pi e}{\hbar c}\,\frac{1}{A_n} \qquad 1.7$$

which is the Onsager relation (Equation 1.1) provided that $A_n = A_{ext}$. The quantized k-space orbits of Equation 1.6 are shown in Figure 1.2 for a fixed magnetic field value. These orbits are confined to the cylinders oriented along k_z, for H parallel to z. Also shown in this figure is a hypothetical, ellipsoidal Fermi surface. Recall that all quasiparticles must reside within this constant energy surface, and furthermore, are now required by Bohr-Sommerfeld quantization to be distributed on the highly degenerate Landau levels within the Fermi surface, for $H \neq 0$. From Equation 1.6 we see that as the magnetic field intensity is increased, the k-space orbits will also increase in area and move toward the FS. When one of the orbital areas, say A_n, passes through the Fermi surface at an extremal FS point, a maximum number of quasiparticles on that level must simultaneously make transitions to lower area Landau levels. This requires the free energy of the particle system as a whole to change abruptly when $A_n = A_{ext}$. In addition, these energy changes are spaced equal increments of 1/H apart. Thus, with the substitution of $A_n = A_{ext}$ in Equation 1.7 we have the Onsager relation (Equation 1.1).

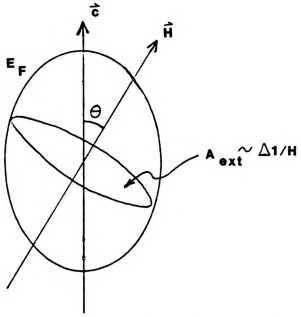

Figure 1.1 Extremal cross section of an elliptical FS segment.

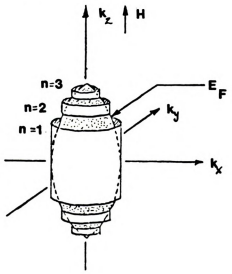

Figure 1.2 Elliptical FS segment and Landau levels.

A general and formal result for the oscillatory free energy of a Bloch electron gas, derived by Lifshitz and Kosevitch is,[3]

$$F_{osc} = \frac{2Vk_B T\left(\frac{eH}{hc}\right)^{3/2}}{\left|\frac{\partial^2 A(E_F,k_z)}{\partial k_z^2}\right|_{ext}^{1/2}} \qquad 1.8$$

$$\times \sum_{\ell=1}^{\infty} \frac{\cos\left\{\frac{\ell\pi c}{eH} A_{ext}(E_F) - 2\pi\ell\gamma \pm \pi/4\right\}}{\ell^{3/2} \sinh\left(\frac{2\pi^2 \ell k_B T}{\hbar\omega_c^*}\right)}$$

$$\times \cos\left(\frac{\ell\pi g m_c^*}{2m_o}\right) e^{-\pi\ell/\omega_c^*\tau}$$

where,

V is the volume of the system

T is the temperature in K

$\left|\frac{\partial^2 A(E_F,k_z)}{\partial k_z^2}\right|_{ext}^{1/2}$ is the curvature of the Fermi surface along the field direction, evaluated at the extremum.

m_c^* is the cyclotron effective mass = $h^2/2\pi \left.\frac{\partial A}{\partial E}\right|_{E_F, ext}$

$\omega_c^* = \frac{eH}{m_c^* c}$

γ is a phase constant, $\simeq \frac{1}{2}$ (quadratic dispersion relation)

g is the spectroscopic spin splitting factor $\simeq 2$

τ is the life time of a state on the extremal cross section of FS

ℓ is the index for the ℓ^{th} harmonic.

This equation is valid under the following conditions:

$\omega_c^* \hbar << E_f$, $k_B T << E_f, F/H >> 1$.

Where $F = \frac{\hbar c}{2\pi e} A_{ext}$.

Typically, we will be interested only in the fundamental, i.e. $\ell = 1$ term of Equation 1.8. The factor $e^{-\pi \ell/\omega_c^* \tau}$ was originally derived by Dingle and accounts for collision broadening of the levels.[6] The $\cos(\frac{\ell \pi g m_c^*}{2m_o})$ factor is due to particle spin.[7] Note: when gm_c^*/m_o = 1,3,5..., the amplitude of the fundamental frequency will vanish.

1.3.2 Thermodynamic Analysis

The formal result of Lifshitz and Kosevitch is now used in a thermodynamic analysis to obtain a working expression for the MTO technique. Using an outline of the argument from reference 8, we obtain an expression for the oscillatory lattice temperature of an isolated metallic solid.

The simplified system to be analysed is shown in Figure 1.3. The 'sample' consists of the solid under study, plus the sensor to detect the lattice temperature, and any other thermal loading by the sample support, wiring, and etc. The specific heat of the sample c_H includes all these contributions, as well as the sample's specific heat. We include in the analysis effects of a thermal link (dQ in Figure 1.3) between the sample, and thermal reservoir (cryostat). This thermal link is required to maintain an ambient sample temperature, otherwise dissipation in the MTO sensor and eddy current heating during magnetic field

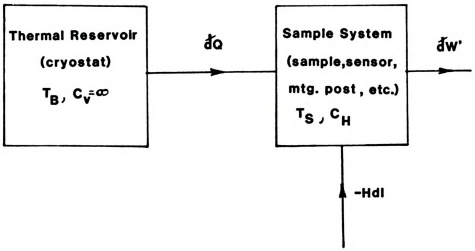

dQ is positive for heat flow into the sample system

dW' is positive for work done by the system

Figure 1.3 Thermodynamic system.

changes would cause a temperature increase. The thermal link is also needed for initial cooling of the sample. The abridged form of the thermodynamic analysis of our ideal system follows. The first law of thermodynamics,

$$đQ = dU + đW$$

becomes 1.9

$$đQ = dU + đW' - HdI$$

for a magnetic system. We consider H and T as independent variables. đQ is positive for heat flow into the sample, đW' is positive for work done by the system, and represents Joule and eddy current heating. The term -HdI is the work done by the magnetic field, and is related to the oscillatory free energy. Using simple thermodynamic relations, Equation 1.9 can be rewritten as,[8]

$$dQ = C_H dT + T \left(\frac{\partial I}{\partial T}\right)_H dH + dW' \qquad 1.10$$

where c_H is the heat capacity of the sample, and $T = T_s$ is the sample temperature. The heat flow through the thermal link (dQ/dt) is then due to dissipative effects, dW', and the oscillatory lattice temperature from the MTO. If K is the thermal conductivity of thermal link, then

$$\frac{dQ}{dt} = -K(T_s - T_B) = -K\delta T \,. \qquad 1.11$$

Taking the time derivative of Equation 1.10, and using Equation 1.11,

$$-K\delta T = C_H \frac{d(\delta T)}{dt} + T_s \left(\frac{\partial I}{\partial T}\right)_H \frac{dH}{dt} + \frac{dW'}{dt} \qquad 1.12$$

where we have used T_B = constant so that $dT_s/dt = d(\partial T)/dt$.

We now use the result of Lifshitz and Kosevitch for F_{osc} to calculate $dI/dT)_H$ by using $I = 1/V \left(\frac{\partial F_{osc}}{\partial H}\right)_T$. We obtain,

$$\left(\frac{\partial I_{osc}}{\partial T}\right)_H = - \frac{A_\ell 2\pi F_\ell}{H^{1/2}} \sin\left\{\frac{2\pi F_\ell}{H} + \phi_\ell\right\} e^{-b_\ell T_i/H} \qquad 1.13$$

$$\times \frac{b_\ell T/H \coth(b_\ell T/H) - 1}{\sinh b_\ell T/H}$$

which we substitute into Equation 1.12. The first order differential equation 1.12 is difficult to solve as is, but is soluble under the following justified assumptions:

$\delta T/T_s < 1$ so that $T_s \sim$ constant $= T_o$

we evaluate Equation 1.12 at an average field H_o where $H = H_o + \alpha t$

C_H is a constant

K is a constant

dW'/dt is constant $= P$.

Under these assumptions, the working expression for the MTO technique is,

$$\delta T_{osc} + \delta T' = \frac{-2k_B T_o H_o^{3/2} (e/hc)^{3/2}}{C_H \left|\frac{\partial^2 A(E_F, k_z)}{\partial k_z^2}\right|_{ext.}^{1/2}} \qquad 1.14$$

$$\sum_{\ell=1}^{\infty} \left\{ \frac{\sin\left\{\frac{2\pi F_L}{H} - 2\pi\ell\gamma \pm \frac{\pi}{4} - \tan^{-1}\left(\frac{2\pi T_Q}{\tau_{osc}}\right)\right\}}{\sqrt{1 + (\tau_{osc}/2\pi T_Q)^2}\ \ell^{3/2}} \right.$$

$$\cos\left(\frac{\pi g m_c^* \ell}{2m_o}\right) e^{-b_\ell T_i/H} \left(\frac{b_\ell T_o/H_o \coth(b_\ell T_o/H_o) - 1}{\sinh b_\ell T_o/H_o}\right)\Big\} + P/K + Ce^{-t/\tau_Q}$$

where,

δT_{osc} = oscillatory lattice temperature due to quantum oscillations.

$\delta T'$ = the lattice temperature change due to effects of dissipative heating, eddy current heating, and the thermal link.

$F_\ell = \left(\frac{\hbar c}{e}\right) \cdot A_{ext}\,(E_F)\ell$ (the Onsager relation)

$$b_\ell = \left(\frac{2\pi^2 k_B m_c^* c}{e\hbar}\right) \ell = 1.47 \times 10^5 \frac{m_c^*}{m_o} \ell \text{ G/K}$$

τ_{osc} = period of dHvA oscillations

τ_Q = thermal time constant of the thermal link = $C_H L/KA$

T_i = Dingle temperature

C = constant

1.3.3 Discussion of the Result

In addition to obtaining the extremal FS cross sections from MTO, additional information can be obtained by analyzing measured amplitudes using the amplitude factors of Equation 1.14.

The factor

$$\left(\frac{1}{1+(\tau_{osc}/2\pi\tau_Q)^2}\right)^{1/2} \qquad 1.15$$

accounts for thermal damping of the MTO amplitude due to the thermal link. For a linear magnetic field sweep, $H \sim t$, τ_{osc} will be a function of magnetic field since the oscillations are periodic not in H,

but in 1/H. Thus, this damping term will not be a constant, and the amplitude as a function of magnetic field will be complicated by the effects of the thermal link, which are not of interest. For 1/H sweeps, (section 2.3) this term is a constant, provided τ_Q is independent of H.

The next factor,

$$\frac{x \coth x - 1}{\sinh x} = A(m_c^*/m_o,\ T,\ H) \qquad 1.16$$

is a function of the cyclotron effective mass through $x = 1.47 \times 10^5 (m_c^*/m_o)T/H$ (G/K), and accounts for thermal broadening of the Landau levels. Figure 1.4 is a plot of this function for an experimentally meaningful range of x values. This function has a weak dependence on x, for x near 1.6. Also shown in this figure is the corresponding amplitude factor for the dHvA effect, 1/3 sinh x, which in general displays a stronger dependence on x over a wider range of x values. The effective mass can be determined by the following method. For a given dHvA frequency the MTO amplitude versus temperature is measured for a chosen magnetic field value H_o. Under the assumption $x \geq 2.0$, (dependent on m_c^*/m_o) for this range of temperatures and H_o, we can approximate Equation 1.16 by

$$2(x-1)e^{-x} \qquad 1.17$$

with an error < 10%, see Figure 1.4. From this, curves of A versus temperature can be generated. The measured amplitude variation with temperature should display the same temperature dependence as the factor 1.17 only for the proper choice of m_c^*/m_o. The temperature dependence of A for various values of m_c^*/m_o is shown in Figure 5.3. The cyclotron effective mass determined from the MTO experiment is $m_c^* = \hbar^2/2\pi\ \partial A/\partial E\big|_{E_F}$.

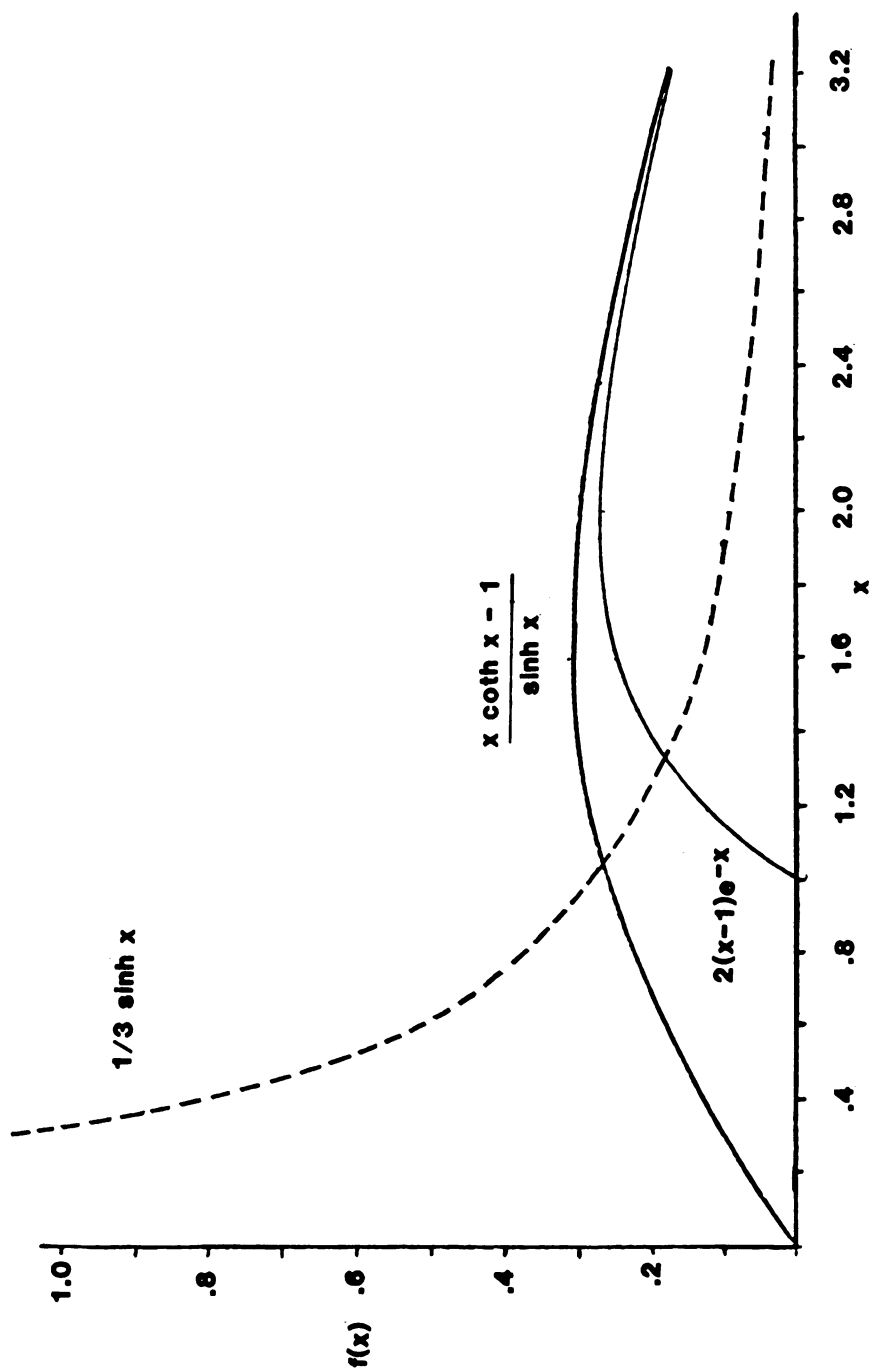

Figure 1.4 MTO and dHvA Amplitude Dependence on m*

$x = 1.47 \times 10^5 \, m_e^*/m_o \cdot T/H$

The factor

$$e^{-b_\ell T_i/H} \qquad 1.18$$

where $b_\ell = 1.47 \times 10^5 \, m_c^*/m_o \, \ell \, (G/K)$,

represents effects of collisions which attenuate the amplitude, and was first included in the dHvA theory by Dingle.[6] The relation between the lifetime τ of the orbit, and T_i, the Dingle temperature, is given by

$$T_i = \hbar/(2\pi k_B \tau). \qquad 1.19$$

For a measured value of m_c^* we may determine T_i for the same orbit from a plot of $\ln(\delta T/H^{3/2})$ versus $1/H$ at constant temperature. At a fixed temperature Equation 1.14 gives

$$\ln \delta T/H^{3/2} = \text{constant} - \left[1.47 \times 10^5 \left(\frac{m_c^*}{m_o}\right)\right] T_i/H \qquad 1.20$$

so that T_i is given by the slope of the above graph.

1.4 General Comments

Given our MTO expression 1.14 and its interpretation in section 1.3.3 we can now obtain the size and topology of the FS, as well as the effective masses and Dingle temperatures. The dHvA effect and the related MTO and SdH effects have been proven to be the most powerful techniques available for deducing the geometry of the Fermi surface. Note that the MTO equation applies to an individual Fermi surface segment, but the experiment will measure $\Delta T = \sum_i (\delta T)_i$ where the index i identifies the i^{th} segment of the FS. Hence, identification of individual FS segments requires Fourier analysis of the MTO signal.

CHAPTER TWO

EXPERIMENTAL METHOD

2.1 Introduction

A simplified version of the expression for magnetothermal oscillations (MTO) is (see Equation 1.14):

$$\delta T = \sum_i A_i(T,\theta,H) \sin\left(\frac{2\pi F_i(\theta)}{H}\right) . \qquad 2.1$$

To observe MTO the magnetic field H is swept continuously and the resulting oscillations of the lattice temperature are detected. The frequency of these oscillations, $F_i(\theta)$, the de Haas-van Alphen frequency, is related to an extremal cross section of the i^{th} segment of the Fermi surface (FS) through the Onsager relation, Equation 1.1. A complete description of the geometry of the FS can be obtained by observing the dependence of $F_i(\theta)$ on θ, the angle between the sample c-axis (for example) and the magnetic field direction. The amplitude A_i of the i^{th} orbit is a function of the magnitude of the magnetic field, the sample's perfection, its average temperature, and the angle θ. Additional amplitude dependence of δT comes from many sources; e.g., the time rate of change of the magnetic field, the sample size, thermal links between the sample and its thermal environment, and so on. Additional FS information may be obtained from the amplitude factor A_i, which is a function of the effective mass, m_c^*, of carrier i, and its Dingle temperature T_i. From the temperature dependence of the amplitudes A_i, the effective masses can be found. Following the discus-

sion in section 1.3.3, the effective mass can be determined by matching the temperature dependence of A as calculated from Equation 1.17 with the observed dependence by adjusting the value of m_c^*/m_o. This procedure is well justified under the condition, m_c^*/m_o (T/H) 1.47 x 10^5 > 2. The Dingle temperature T_i represents the effects of collisions of the i^{th} carrier. To obtain T_i, the field dependence of the amplitude at fixed temperature is measured. For 1/H sweeps (see section 2.3), T_i can be obtained from a plot of $\ell n(\delta T/H^{3/2})$ versus 1/H, which should yield a straight line whose slope is proportional to T_i (Equation 1.20).

Before presenting and discussing the experimental cryostat designed to observe MTO, we review its design requirements in light of the above: (1) MTO is observable only at low temperatures, (2) the MTO sensors must have a sensitivity of ~ 10^{-6}K, (3) thermal loading of the sample by the sensor must be minimal, (4) the sample must be thermally isolated, (5) sample orientation relative to the field must be adjustable, and (6) the ambient temperature must be adjustable.

2.2 Experimental Cryostat

The cryostat and superconducting solenoid are cooled by a liquid helium bath in a conventional glass dewar. The magnet is hung from a frame mounted on top of the dewar. The cryostat is placed inside the dewar and is also supported by the magnet frame. A schematic of the MTO cryostat used in this research is shown in Figure 2.1. The sample (not shown) is attached, using a low temperature vacuum grease†, to a Vespel* mounting post inside the ring gear. A weak thermal link (#46 copper

†Apiezon "N grease," Apiezon Product Ltd.
*A low thermal conductivity, low specific heat resin made by Dupont Company.

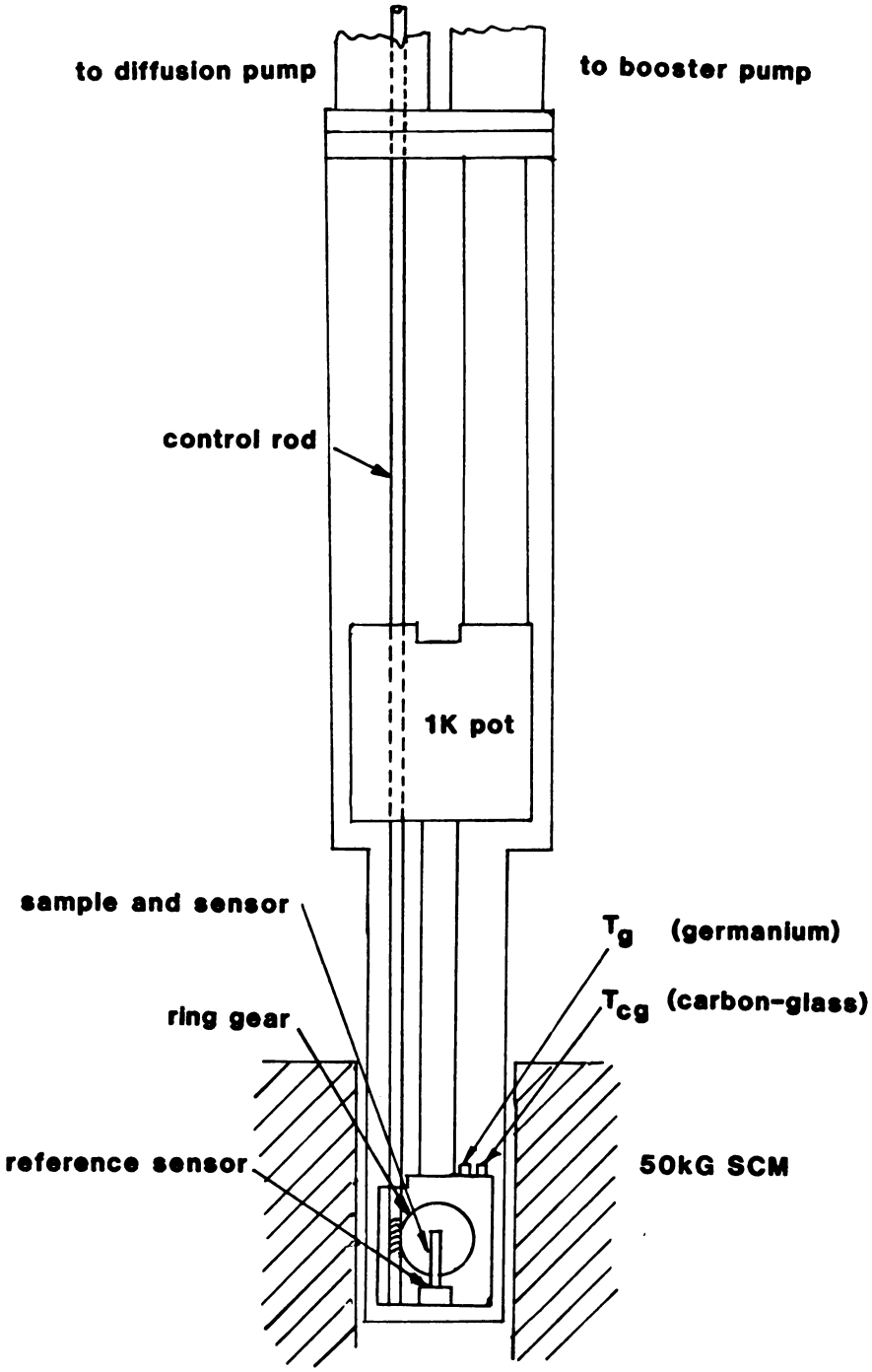

Figure 2.1 The MTO Cryostat.

wire) between the sample and cryostat compensates for eddy current heating and provides a means for obtaining ambient equilibrium. The sample is otherwise thermally isolated once the cryostat has been evacuated to ~ .5 x 10^{-6} Torr. The ring gear and sample can be rotated through 90° relative to the vertical magnetic field direction by turning the control rod shaft. From the known gear ratios, the angular position can be reproduced to within ±0.3° using a revolution counter. The control rod passes through and is thermally lagged at the '1K pot' and again at the 4K flange, see Figure 2.1. The rod continues up the vacuum pumping line and terminates above an O-ring seal where the counter is situated. The 1K pot is a chamber which holds 250 ml of liquid helium and is filled via a needle valve. This chamber is in thermal contact with the sample region and can be cooled to .9K by evaporation of the helium using booster and mechanical pumps. The sample region temperature is monitored by a factory-calibrated germanium resistance thermometer† and a four-wire conductance bridge. A second thermometer, which has a weak magnetic field dependence,* is used in a resistance heater feedback loop which can provide stable temperatures between 10 and .9K. The heater is a 100 Ohm chip resistor which is in contact with the 1K pot. The 4K flange serves, in part, to cool the electrical wiring to 4K. The wiring consists of #40 copper (current leads) and #40 manganin (potential leads) wires. The heat loss between the 1K pot and 4K flange is about 20mW.

†Lake Shore Cryogenics GR-200A-100. Factory calibrated .3-6.0 K.
*Lake Shore Cryogenics CGR-1-1000. Field dependence .5 T/T (%) at 8T.

2.3 Magnetic Field

The magnetic field is produced by a 50kG niobium-titanium superconducting solenoid.† Field homogeneity is $\lesssim .1\%$ within 1" of the winding center. The magnetic field to energizing current ratio for this magnet is 848.9 Gauss per Ampere. This value was confirmed using an NMR probe,[9] and by performing experiments on a test sample (section 5.2.1).

The magnetic field may be swept in a linear mode, $H \sim t$, or in a 1/H mode, $H \sim t^{-1}$. With a linear sweep, the resultant MTO will be aperiodic, as shown in Figure 2.7. Typical linear sweep rates ranged from 0.5 to 10 amperes/minute depending on sample size, temperature, angle, etc. A linear ramp mode was used in acquiring some of the data presented in Chapter 5. The linear ramp was provided by a commercial sweep controller.* Tne remainder of the data, however, was obtained using a 1/H drive. This mode of field sweep has several advantages. The MTO signal is then periodic in real time so that analog filtering can be performed to enhance the signal to noise ratio on selected de Haas-van Alphen frequencies. In addition, the thermal damping factor,

$$\left[\frac{1}{1+(\tau_{osc}/\tau_Q)^2}\right]^{1/2} \qquad 2.2$$

is then a constant. In a linear sweep mode, τ_{osc} is a function of time (or field) so a systematic error in the MTO amplitude dependence on H complicates the analysis of Dingle temperatures. Finally, eddy current heating, which is significant at low magnetic fields, is substantially reduced since the sweep rate is low at small values of H.

†Oxford Instruments Company, Ltd., Model K1034.
*O.S. Walker Company.

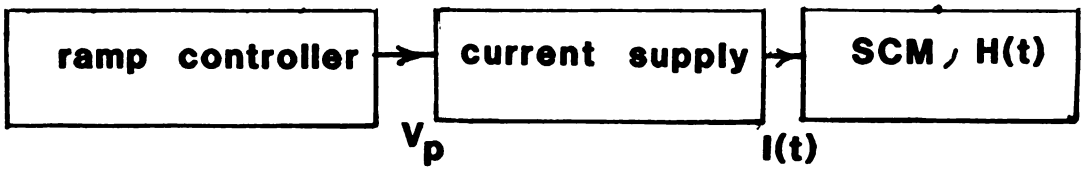

(a)

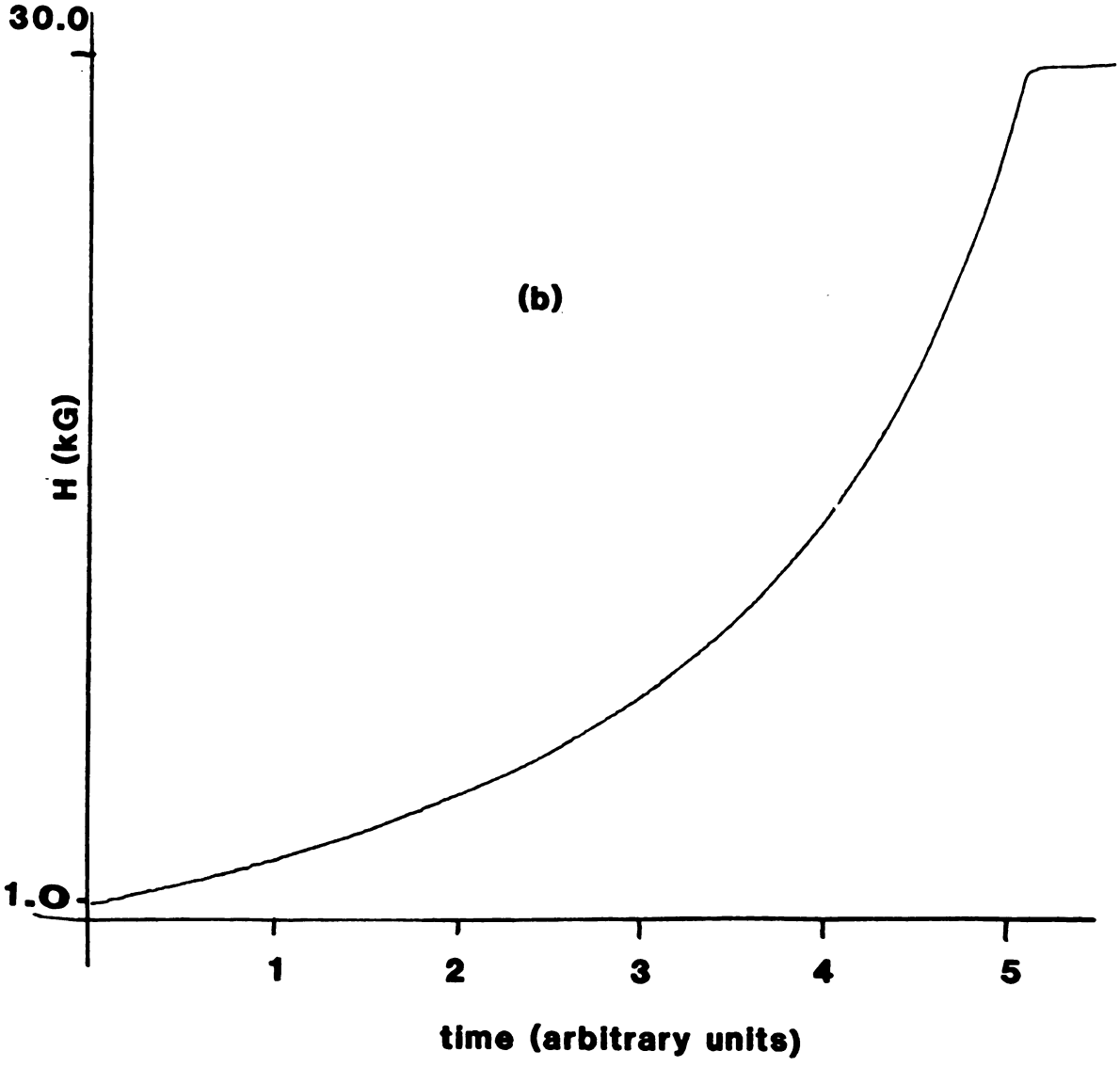

(b)

Figure 2.2 (a) Schematic of the sweep control system.

(b) H vs t for a 1/H sweep.

Figure 2.2(a) is a schematic of the control system for the superconducting magnet. A voltage $V_p(t)$ is generated by the ramp controller and is input to the programmable current supply so that

$$I(t) \sim V_p(t) \qquad 2.3$$

where I(t) is the current through the superconducting solenoid. In a superconducitng solenoid $I \sim H$, so that $H(t) \sim V_p(t)$. To obtain a linear ramp from this system, $V_p(t) = \alpha t$, where α is the sweep rate. If a 1/H sweep is desired, the program voltage should be,

$$V_p \sim \frac{c}{c - \alpha t} \qquad 2.4$$

where c is a constant and $c > \alpha t$. This function has a time dependence such that equal increments in $1/V_p$ (i.e. 1/H) occur in equal time intervals, as required to give a periodic MTO signal. The commercial linear ramp controller was modified to produce a program voltage which approximates Equation 2.4. In Figure 2.2(b) the magnetic field versus time obtained by using the modified sweep controller is shown. The output shown in that figure deviates less than 4% from a true 1/H sweep over wide ranges (> 20kG) of magnetic field.

2.4 Measuring Small Temperature Oscillations

Typical magnitudes of δT in Equation 2.1 are of order 10^{-4}K. The method used, capable of detecting temperature changes as small as .5 x 10^{-6}K, employs an A.C. bridge circuit and small carbon composition resistors.

Carbon composition resistors have a resistance-versus-temperature relation at low temperatures given by

$$R = e^{(A/T + B)} \text{ or } dR/dT \sim \frac{e^{A/T}}{T^2} ; \quad T \text{ in K.} \qquad 2.5$$

For the resistors chosen for this research, A = 5.24K and B = 6.43.† At ambient temperatures near 1K a temperature change of 10^{-6}K corresponds to a resistance change of a few Ohms. The carbon resistors also have a small specific heat; as mentioned earlier, a small heat capacity prevents damping of the MTO signal by thermal loading. Two resistors, matched in resistance-versus-temperature characteristics to ~ 1% from room temperature to 4.2K were used in the differential input bridge circuit described below.

We wish to detect temperature oscillations δT about the ambient sample temperature. To this end we use two resistors; one, R_s, in thermal contact with the sample; the other, R_r, attached to the sample region of the cryostat. We detect MTO by measuring the resistance difference between the two thermometers while sweeping the magnetic field. From Equation 2.5 the oscillatory resistance difference must be proportional to δT if $\delta T \ll T$.

Figure 2.3 is a schematic of the bridge circuit. It consists of a lock-in amplifier, a ratio transformer, and two independent and isolated current supplies. An excitation voltage of frequency ω (117.5 Hz) is supplied to the primary side of the ratio transformer. There are two isolated secondary windings labeled N and Nβ. The secondary windings

†82 Ohm Ohmite "Little Devil" carbon composition resistors lapped to .2mm thick, weight ~.01 grams.

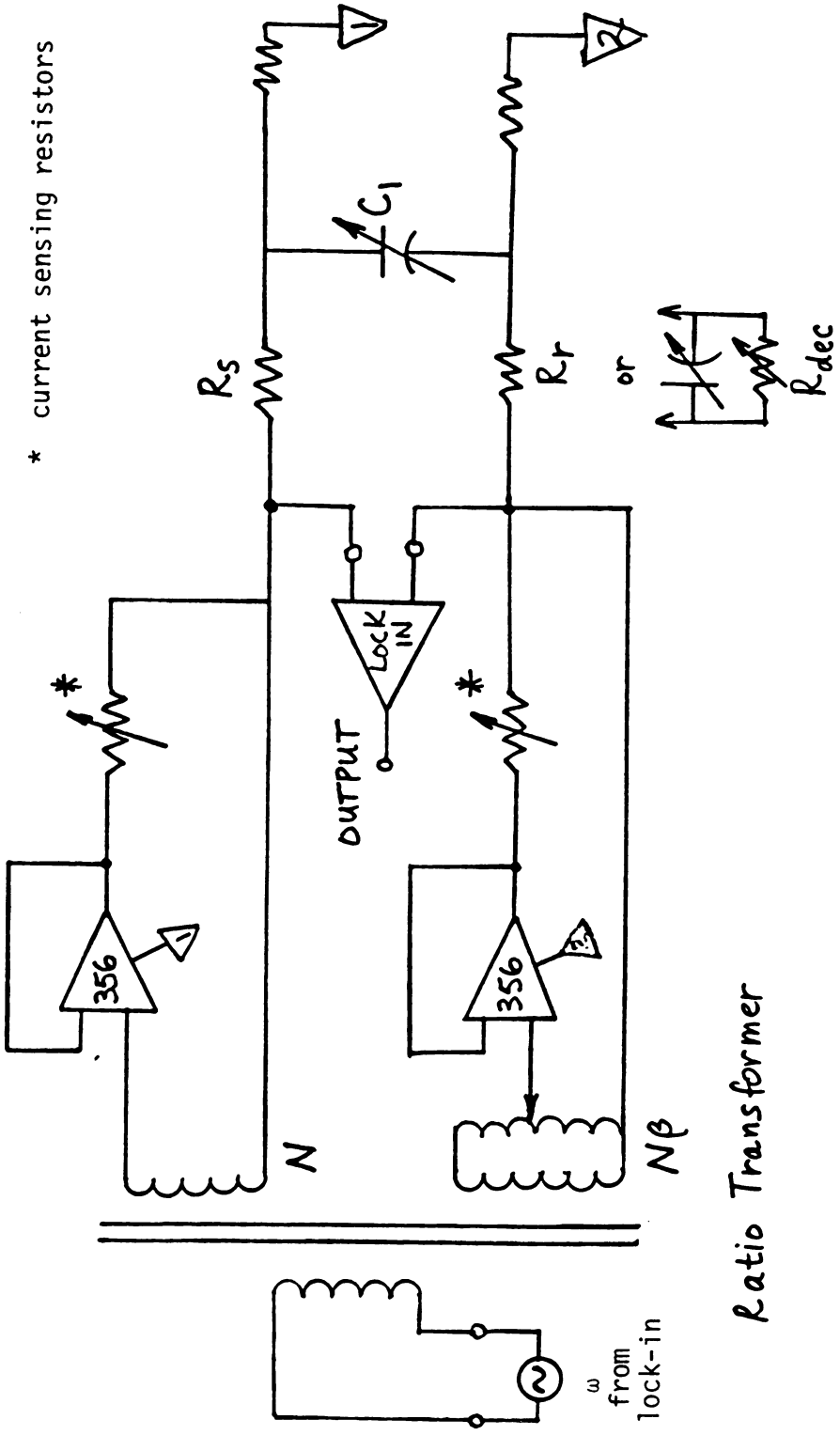

Figure 2.3 Schematic of the A.C. Bridge Circuit.

provide input to the matched and isolated current supply operational amplifiers. The secondary winding Nβ can be stepped from .0001 to 1.2000 times the number of windings on the other secondary, N. Under conditions of zero magnetic field and thermal equilibrium between the sample and the cryostat sample area, the currents I_s and I_r through the resistors are adjusted by changing β until the voltage drop across both resistors is the same. The voltage drop across each resistor is brought from the cryostat (two leads each) to a differential input preamplifier. The combination of the differential input preamplifier and tuned lock-in amplifier measures the resistance difference between R_s and R_r. Once I_s and I_r are adjusted as discussed above, the bridge is in balance and its output is zero. The balance condition may be written,

$$\begin{aligned} I_r &= \beta I_s \\ I_r Z_r &= I_s Z_s \end{aligned} \qquad 2.6$$

where Z_s and Z_r are the impedances of the resistor networks. Note that in addition to adjusting β it may be necessary to adjust c_1, (Figure 2.3), to assure capacitive balance, which is monitored by an oscilloscope. With the conditions of capacitive and resistive balance met, we obtain from Equations 2.6,

$$\beta = R_s/R_r. \qquad 2.7$$

Sweeping the magnetic field then results in an oscillatory lock-in amplifier output due to MTO. The sample temperature, T, may be measured by replacing R_r with a variable reference resistor (via a front panel switch) and adjusting the reference resistor and a variable capacitor until a balance condition is met. To avoid self-heating in the sensors the currents I_r and I_s must be adjusted using the "current sensing

resistors" shown in Figure 2.3. The power dissipation in the sensors should be $\lesssim 10^{-14}$W. Finally, the actual balance condition is

$$\frac{R_s}{1+\omega R_s C_s} = \frac{\beta R_r}{1+\omega R_r C_r} \qquad 2.8$$

thus, ωRC must be less than 1. For very low temperatures where R_s and R_r are large, ω may have to be small (10-30 Hz).

2.5 Data Acquisition and Analysis

A minicomputer[†] was interfaced to the MTO setup for data acquisition and analysis. Figure 2.4 is a block diagram of the interface. The data consists of a set of magnetic field values and their corresponding δR values. The magnetic field value is monitored by a digital voltmeter which reads the voltage drop across a calibrated reference resistor in series with the superconducting solenoid. The sample lattice temperature δT is proportional to the lock-in amplifier output, δR. This output is also analog filtered[*] to enhance the signal to noise ratio on chosen FS orbits, as well as to assure cut off of frequencies higher than the maximum frequency of the fast Fourier transform range, which is given later in this section. The outputs from the analog filter and voltmeter are passed through analog to digital converters prior to input to the computer.

An MTO scan is performed as follows. The user determines the de Haas-van Alphen (or fast Fourier transform) frequency range to be covered. This frequency range is from 0 to

[†]Digital Equipment Corporation PDP 8/e; 32K core, RK05 magnetic disc drive.

[*]Krohn-Hite active filter model #3750 with high, low, and band-pass capabilities.

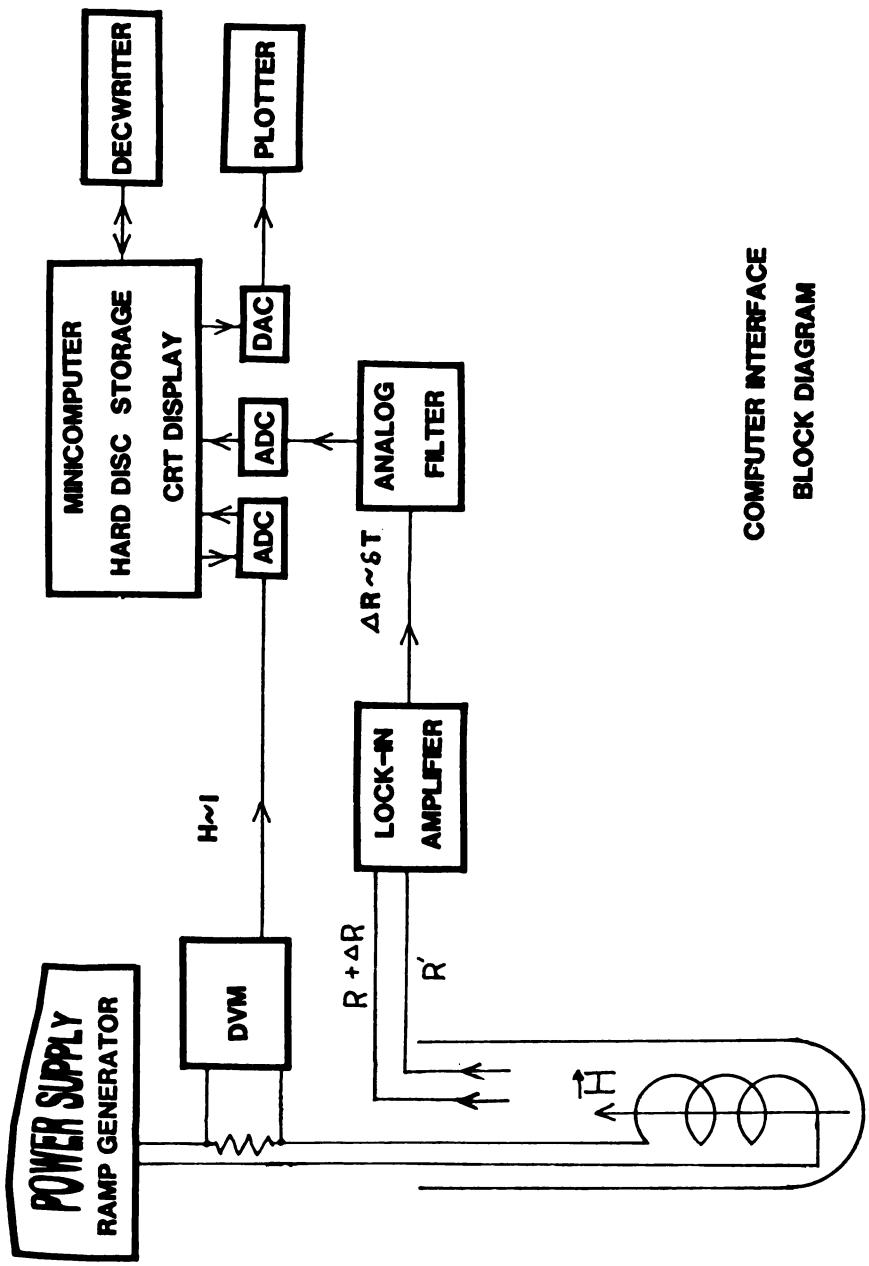

Figure 2.4 Computer Interface Block Diagram.

$$\frac{1}{\left(\frac{1}{H_i} - \frac{1}{H_f}\right)} \text{(file length)} \quad [G] \qquad 2.9$$

where H_i and H_f are the beginning and ending magnetic field values, and the file length is the number of δT and H pairs to be used (typically 512). The computer requests H_i and H_f for each scan, and from these values generates a table of magnetic field values (512) which are equal increments of 1/H apart. During an MTO scan, the current magnetic field value, read by the voltmeter, is compared with the computer generated field value table and when the values agree, a reading is made from the output of the analog filter (δT) and stored in a local computer file. By taking δT readings equal increments of 1/H apart, the stored data appears to be periodic, see Equation 2.1. The local file consisting of (512) δT and H values can be stored in a permanent file on a magnetic disc, see for example Figure 2.5. This set of periodic data can then be fast Fourier transformed to obtain F_i in Equation 2.1, as shown in Figure 2.6. Note that we have essentially converted Equation 2.1 to $\sin(2\pi F_i x) \sim \delta T$ and then Fourier transformed to obtain F_i. The transformed data (or the raw data) can be displayed on a CRT, plotted on an interfaced chart recorder, or printed at a terminal in digital form. The fast Fourier transform program used can be found in references 10 and 11, which also includes a discussion of the derivation, use, and limitations of the fast Fourier transform technique. As mentioned earlier, the δT readings are analog filtered, in part, to cut off frequencies beyond the maximum of the transform range (given by Equation 2.9). A complete discussion of this requirement is found in reference 10. Details concerning the general use of the computer interface can be

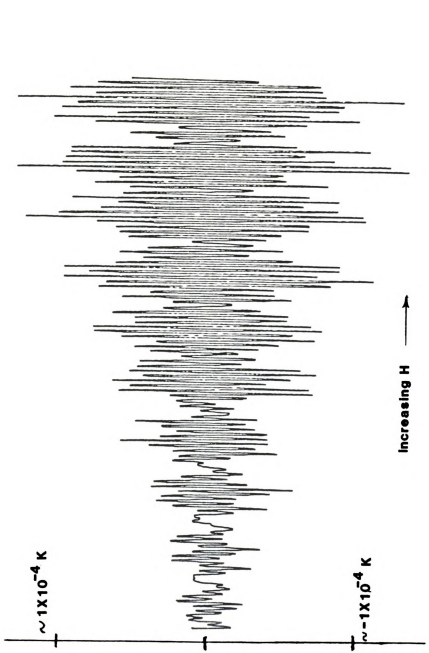

Figure 2.5 MTO Data, Stage 4 $SbCl_5$.

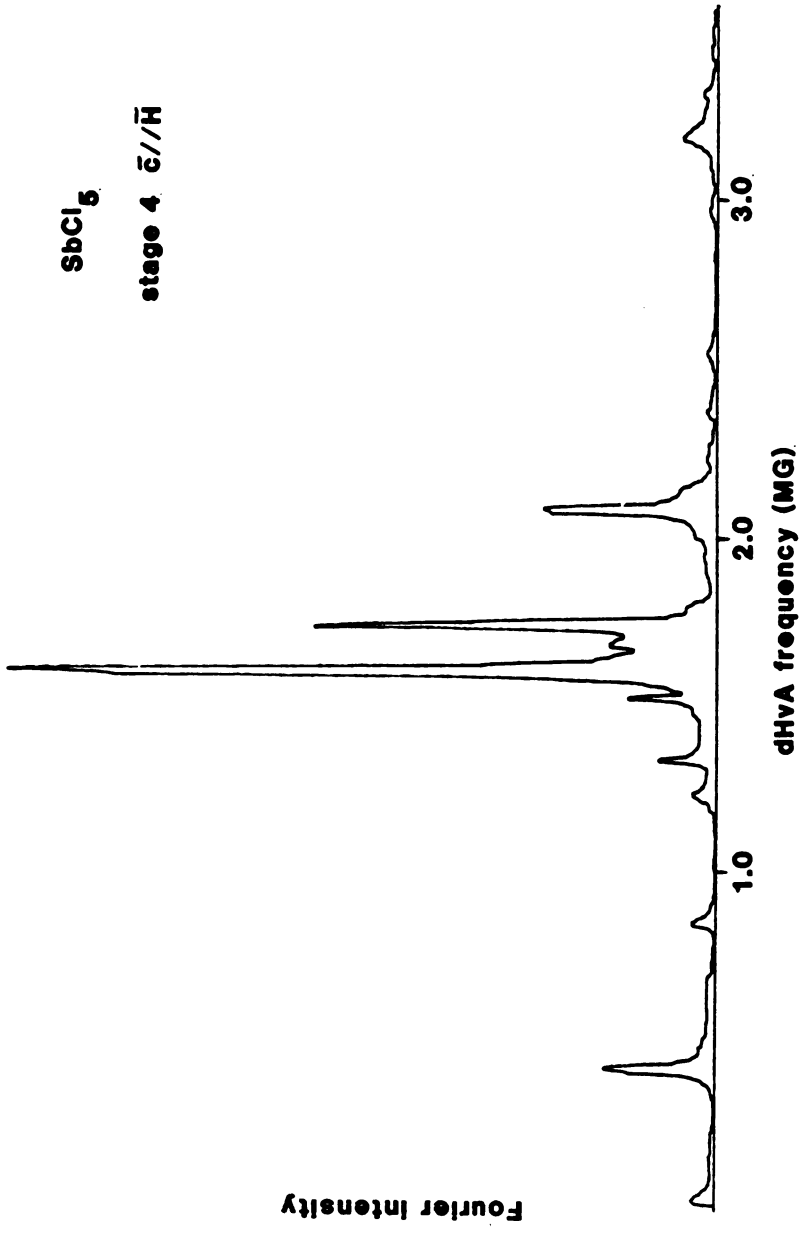

Figure 2.6 Fourier Transformed Stage 4 Data.

found in a reference manual which accompanies the MTO experimental apparatus. The use of this method for data acquisition and analysis has several distinct advantages over earlier, manual methods (see reference 8). First, the stored MTO data can be recovered when desired. Second, the MTO data can be transformed (~ 70 seconds) while the experiment is in progress, giving immediate feedback about the FS data accumulated. Also, the fast Fourier transform program is sensitive to small harmonic components which might otherwise be missed.

MTO data can be taken in a manual mode as well (Figure 2.7). Here the horizontal axis corresponds to magnetic field and the vertical axis is the output of the analog filter. A manual scan is useful for MTO amplitude determination of the effective mass and Dingle temperature for each orbit. Prior to computer assisted data acquisition, a manual scan can be performed to optimize the experimental parameters such as the magnetic field sweep rate, amplifier gain, analog filter characteristics, and determination of H_i, and H_f for the desired dHvA frequency range. The manual data can also be hand transformed to verify the frequencies indicated by the fast Fourier transform program.

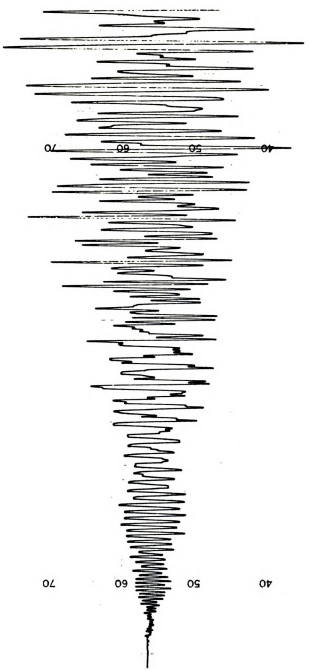

Figure 2.7 MTO Data Taken in the Manual Mode.
Stage 5, 0 to 17.5 kG.

CHAPTER THREE

PROPERTIES AND SYNTHESIS OF GRAPHITE INTERCALATION COMPOUNDS

3.1 Introduction

The first section of this chapter will describe briefly the nature of graphite intercalation compounds. The remainder of the chapter will detail the preparation and structural characterization of the $SbCl_5$ compounds used in this research.

3.2 Review of Graphite Intercalation Compounds

Graphite intercalation compounds consist of the host material, graphite, and atoms, ions, or molecules called the intercalant. The graphite host structure used in this research is the hexagonal form shown in Figure 3.1, with layers of hexagonal rings of carbon atoms stacked in a sequence ABAB. This material is referred to as highly oriented pyrolytic graphite, or HOPG. It is synthetically prepared and consists of layers of crystallites (~ 1μm), which are aligned along the c-axis direction, but not in the basal plane. Within each crystallite, however, there is c-axis and basal plane order.

Through the process of intercalation, whole layers of the intercalant material are ingested into the interlayer spaces between the hexagonal carbon planes. In an ideal compound, an ordered structure occurs along the c-axis and in the intercalant basal plane. The

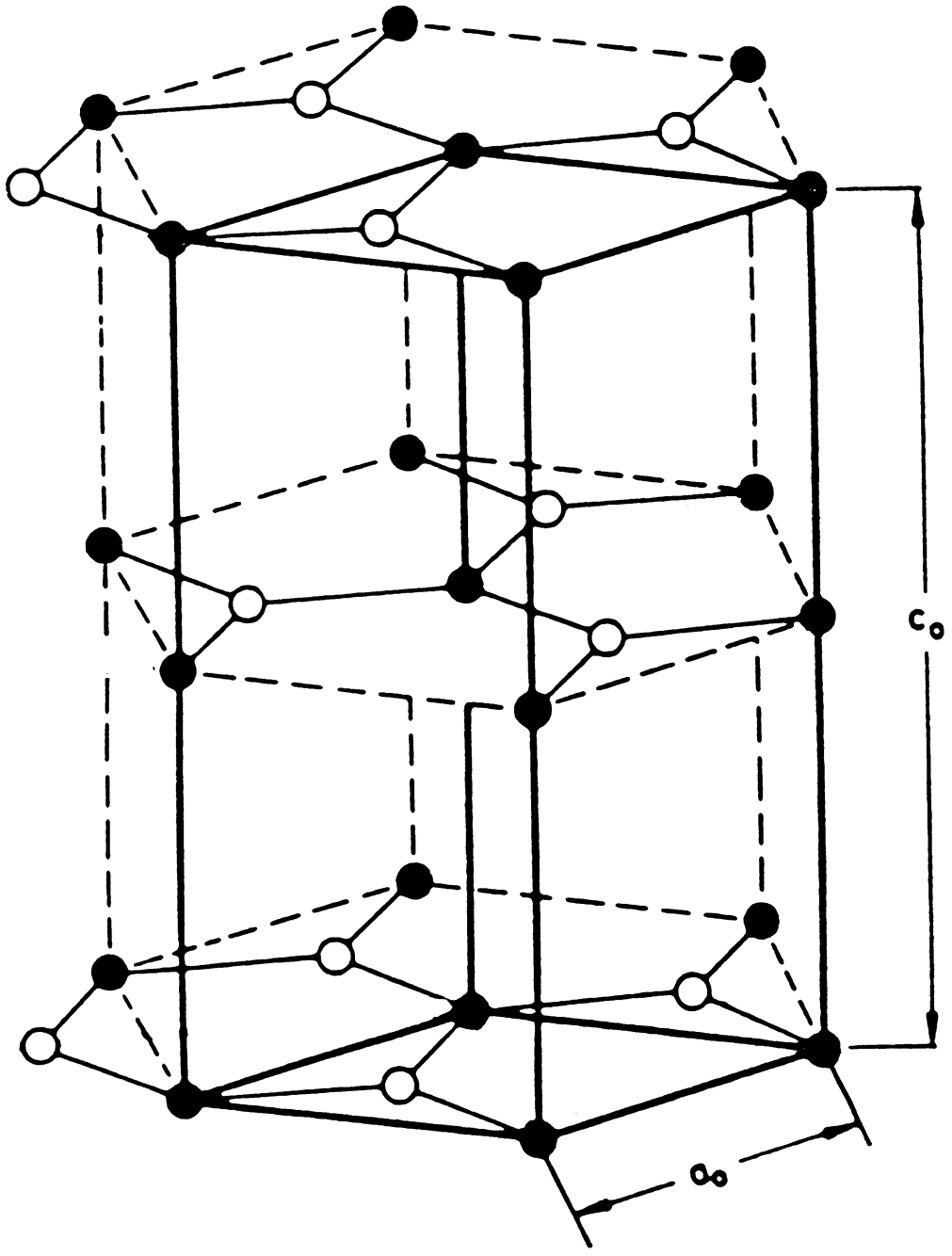

Figure 3.1 Schematic of the Hexagonal Form of Graphite (HOPG).
a_o=2.45 Å, c_o=6.70 Å

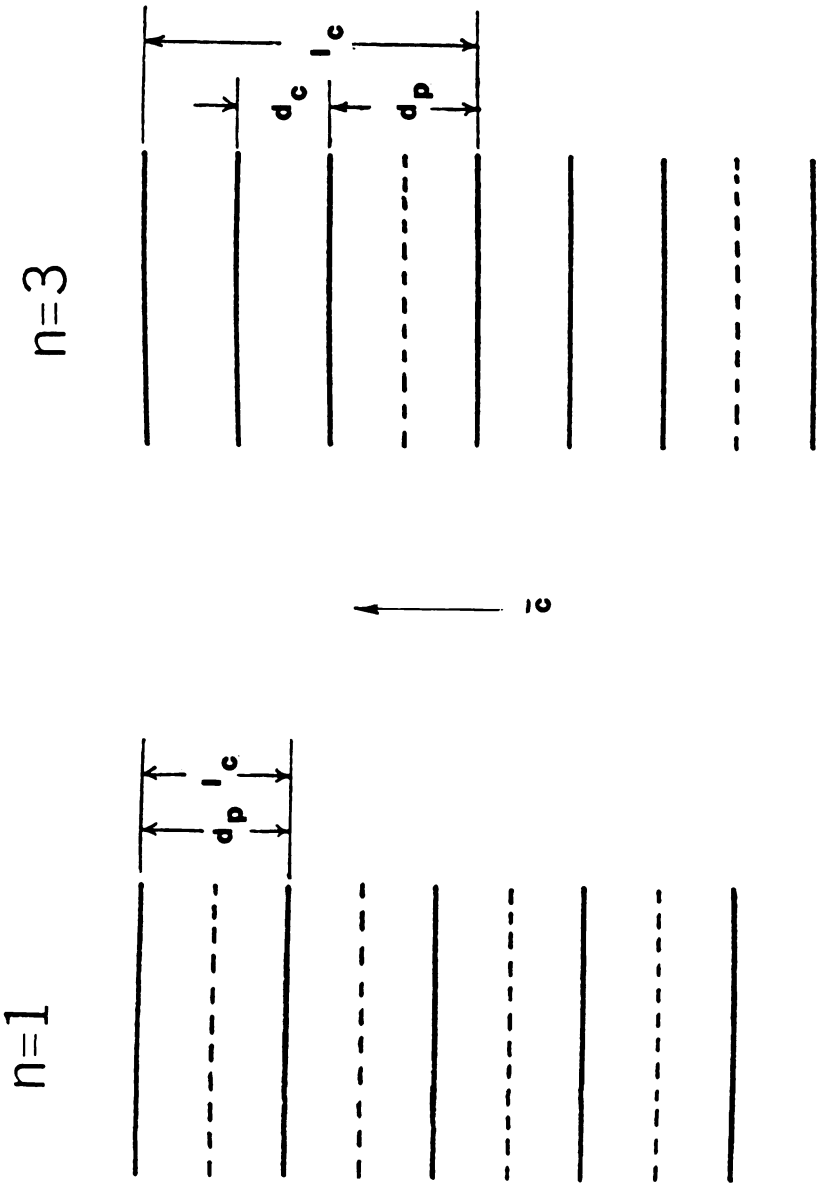

Figure 3.2 Schematic of Staging. Solid lines represent carbon layers, dashed lines represent intercalant layers.

structure along the c-axis is characterized by a staging index n (Figure 3.2). A stage n compound is one in which nearest intercalant layers are separated by n carbon layers. In a simple compound, the distance along the c-axis between equivalent layers, I_c, is related to the stage index n by the phenomenological equation,

$$I_c = [(n-1)d_c + d_p] \; ; \quad n = 1, 2, 3... \qquad 3.1$$

where d_c is the distance between carbon layers in HOPG, 3.35 Å, and d_p is the thickness of a packet formed by the intercalant and its bounding carbon layers (Figure 3.2). The graphite and intercalant layers may also exhibit a stacking sequence in the GIC (reference 12). The in-plane structure of a GIC may be ordered as well as shown in Figure 3.3 for $SbCl_5$ compounds. From this structure a layer stoichiometry is determined from the ratio of the number of intercalants in a layer to the number of carbon atoms in a graphite layer. For $SbCl_5$ compounds, the layer stoichiometry is $C_{14}SbCl_5$.

Intercalation compounds are also classified by the nature of the charge exchange between the graphite layers and the intercalant. In graphite acceptor compounds (GAC's) such as AsF_5 or $SbCl_5$, the intercalant accepts electrons from the graphite layers, leaving them with some net positive charge while maintaining overall charge neutrality. For graphite donor compounds the reverse is true, the intercalant donates electrons to the graphite planes. The amount of charge transfer is quantified by the charge transfer coefficient, f, defined as the fraction of intercalant atoms or molecules that are ionized.

Graphite in its pristine form is anisotropic in its electrical and thermal transport properties. As an example, the ratio of the basal plane to c-axis conductivity, σ_a/σ_c is about 10^3. In general, this

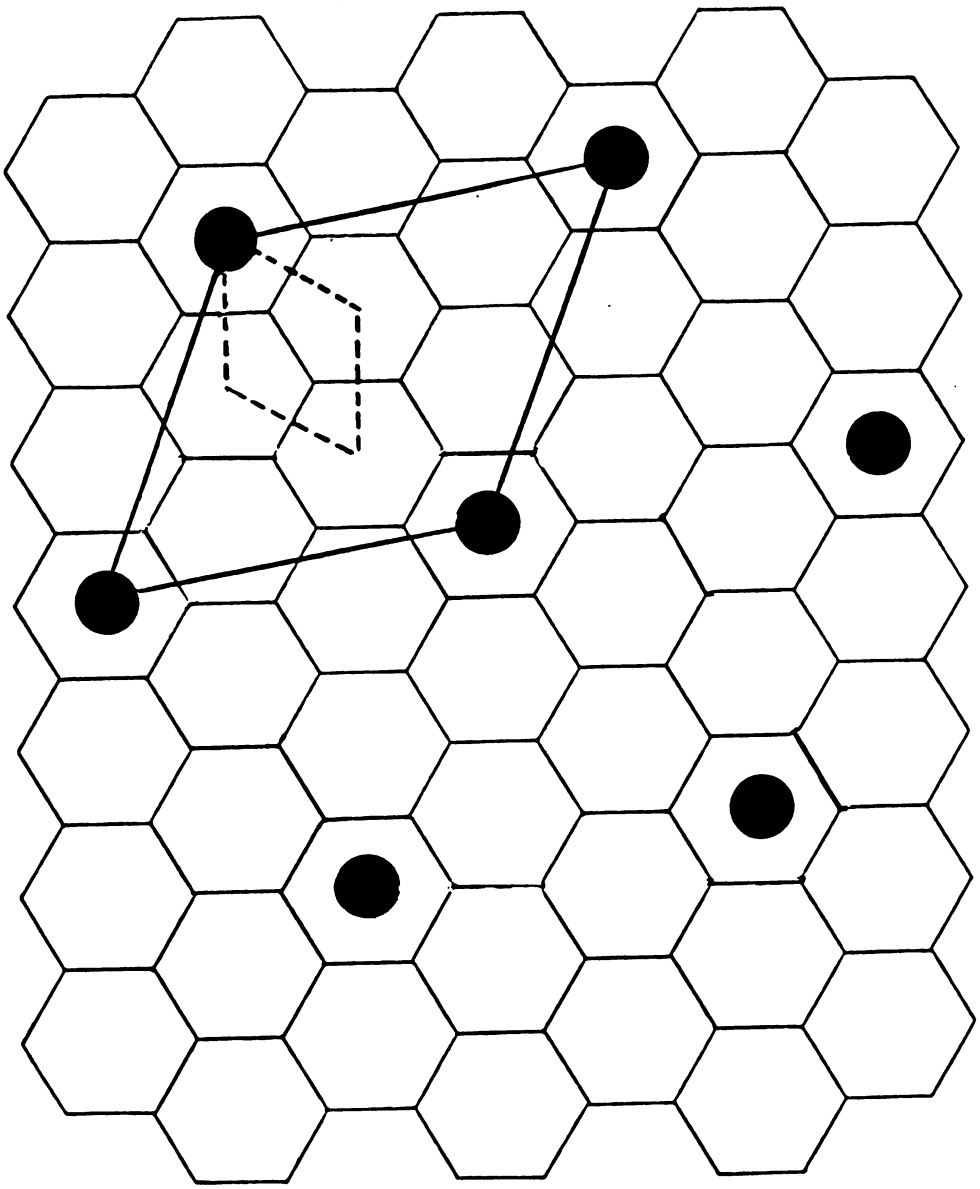

Figure 3.3 Basal Plane Order in $SbCl_5$.

Note: The $\sqrt{7} \times \sqrt{7}$ R19.1° primitive cell for the intercalant is shown in heavy lines, the HOPG primitive cell is shown in dotted lines. A x B Rθ° denotes an intercalant superlattice with primitive translations Aa and Ba where a is the side of the primitive cell of HOPG. The intercalant superlattice is rotated θ degrees relitive to the HOPG cell.

anisotropy is enhanced for acceptor compounds, σ_a/σ_c ranging from about 10^4 to 10^6. For donor compounds, the anisotropy tends to decrease.[13] In both the donor and acceptor compounds, the carrier density (a function of stage) increases from $10^{18}cm^{-3}$ for graphite to $\sim 10^{21}cm^{-3}$ for a typical GIC. Thus, the semimetal graphite is altered to a quasi-metallic state by intercalation. There are several good reviews[12,13] of GIC's available, and the interested reader is referred to them for additional background.

3.3 Preparation of $SbCl_5$ Intercalated HOPG

The HOPG host material† is prepared for intercalation by cutting to a suitable size, typically to 5mm x 10mm x 1mm, using either a diamond impregnated wire saw or a kerosene immersed spark cutter. Next, the HOPG is rinsed with alcohol, placed in an RF furnace and vacuum baked at 1000°C for approximately one hour for cleaning and to remove residues from cutting. The intercalant $SbCl_5$ is a pale yellow liquid at room temperature and will solidify at 2.8°C. The $SbCl_5$ was generally used as provided.* In two cases a vacuum distillation was performed to further purify the $SbCl_5$. However, the GIC's produced with the vendor stock proved to be identical with regard to their physical and electronic structure, and the distillation procedure was discontinued.

Compounds of stage 2, 4, and 5 were produced locally by the two zone vapor transport, or Hérold method.[14] The intercalant and HOPG are placed in a reaction tube, Figure 3.4, inside a glove bag filled with an over-pressure of nitrogen gas. The reaction tube is sealed at the valve

†Provided by A.W. Moore, Union Carbide Corporation.
*J.T. Baker Co. $SbCl_5$ 99.6% purity (carcinogenic).

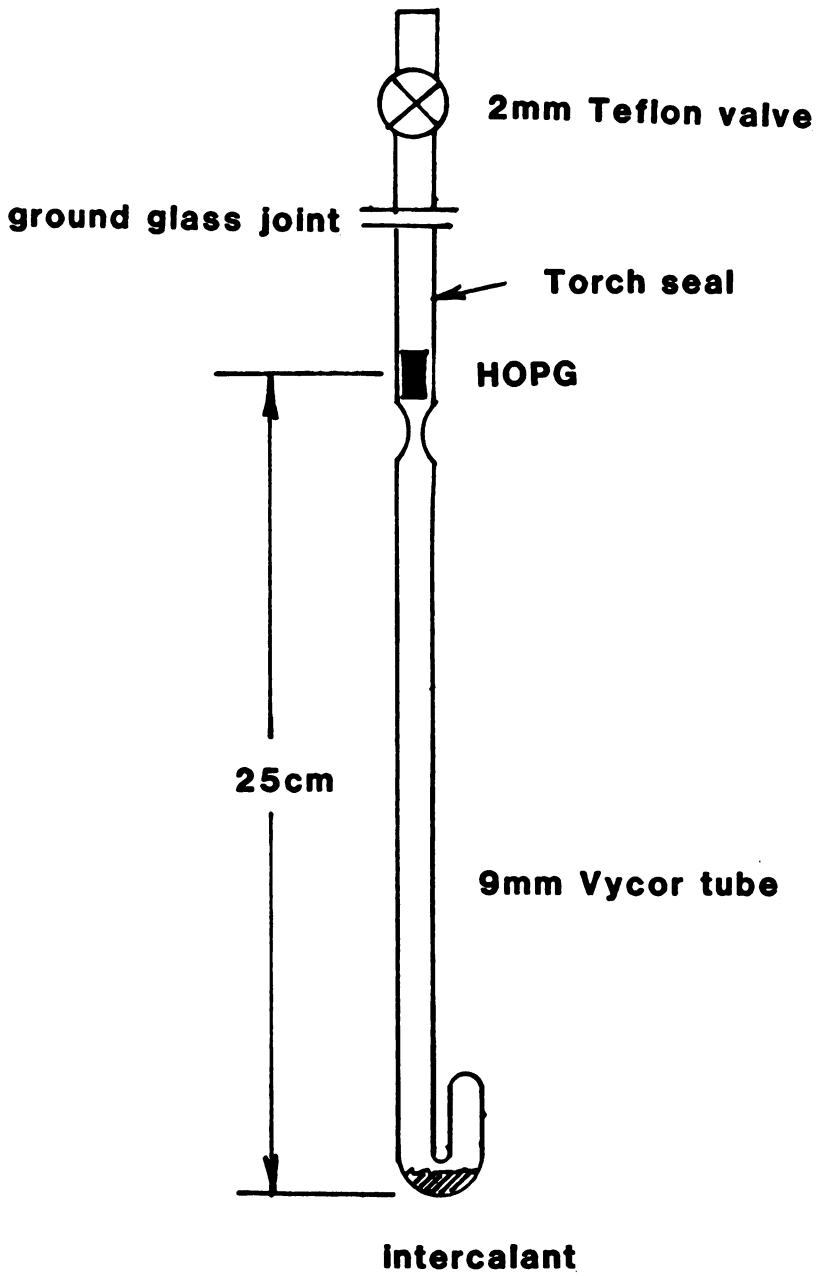

Figure 3.4 Reaction Tube for $SbCl_5$ GIC Synthesis.

after the HOPG and intercalant are loaded, then removed from the glove bag. The $SbCl_5$ is frozen by immersing the reaction tube in liquid nitrogen. The N_2 gas is then pumped off, and glass reaction tube is gas torch sealed (Figure 3.4). The intercalation takes place when the sealed reaction tube is placed in a two zone furnace. The high temperature zone of the furnace controls the temperature of the HOPG, T_g, and the lower temperature zone controls the intercalant temperature, T_I. The stage index of the compound depends on the temperatures T_I and T_g, with the important parameter being $T_I - T_g$. Table 3.1 lists the temperatures required for synthesis of each stage.[15,16]

Table 3.1

Preparation Temperatures and I_c Values for $SbCl_5$ GIC's.[15]

Stage Index n	T_g(C)	T_I(°C)	ΔT	I_c
2	170	115	55	12.72
4	170	70	100	19.42
5	195	75	120	22.77

The furnace was made locally, and the two temperature zones can be "independently" varied between 50 and 950°C ± 1°C. The temperatures T_g and T_I are monitored by Chromel-Alumel thermocouples attached to the outside of the reaction tube next to the graphite and intercalant respectively. Stage equilibrium occurs within about 120 hours.

In addition to the compounds produced locally, the stage 6 and 8 compounds studied were produced by R. Clarke, University of Michigan, using the above technique. The University of Michigan group also provided the stage 1 compound on which measurements were made. Stage 1 $SbCl_5$ compounds are made by the direct immersion method. The intercalant $SbCl_5$ liquid and HOPG are sealed in a reaction tube, with the HOPG immersed in the liquid. The intercalation reaction proceeds at temperatures near 95°C and takes several days.

3.4 Characterization

A uniformly staged compound with a small ($\lesssim 3^0$) c-axis mosaic spread is required for measurement of the stage dependence of the Fermi surface. The c-axis mosaic spread determines the amount of c-axis misalignment of crystallites which form the compound. A large amount of c-axis misalignment will cause broadening of the deHaas-van Alphen frequencies measured for determination of the Fermi surface. The in-plane intercalant superlattice (if any) should also be known, since it is of central importance in one of the GIC Fermi surface models (section 4.3.2).

The stage index and stage fidelity were characterized on all samples before and after Fermi surface measurements. The stage index n is found by measuring and c-axis repeat distance, I_c, and then using Equation 3.1. This repeat distance is obtained from a 00ℓ x-ray diffraction scan, see Figure 3.5, by using the Bragg relation,

$$\ell\lambda = 2I_c \sin\theta \qquad 3.2$$

ℓ = the reflection index for line 00ℓ

θ = the angle for line 00ℓ ($\vec{c}$-axis to x-ray beam)

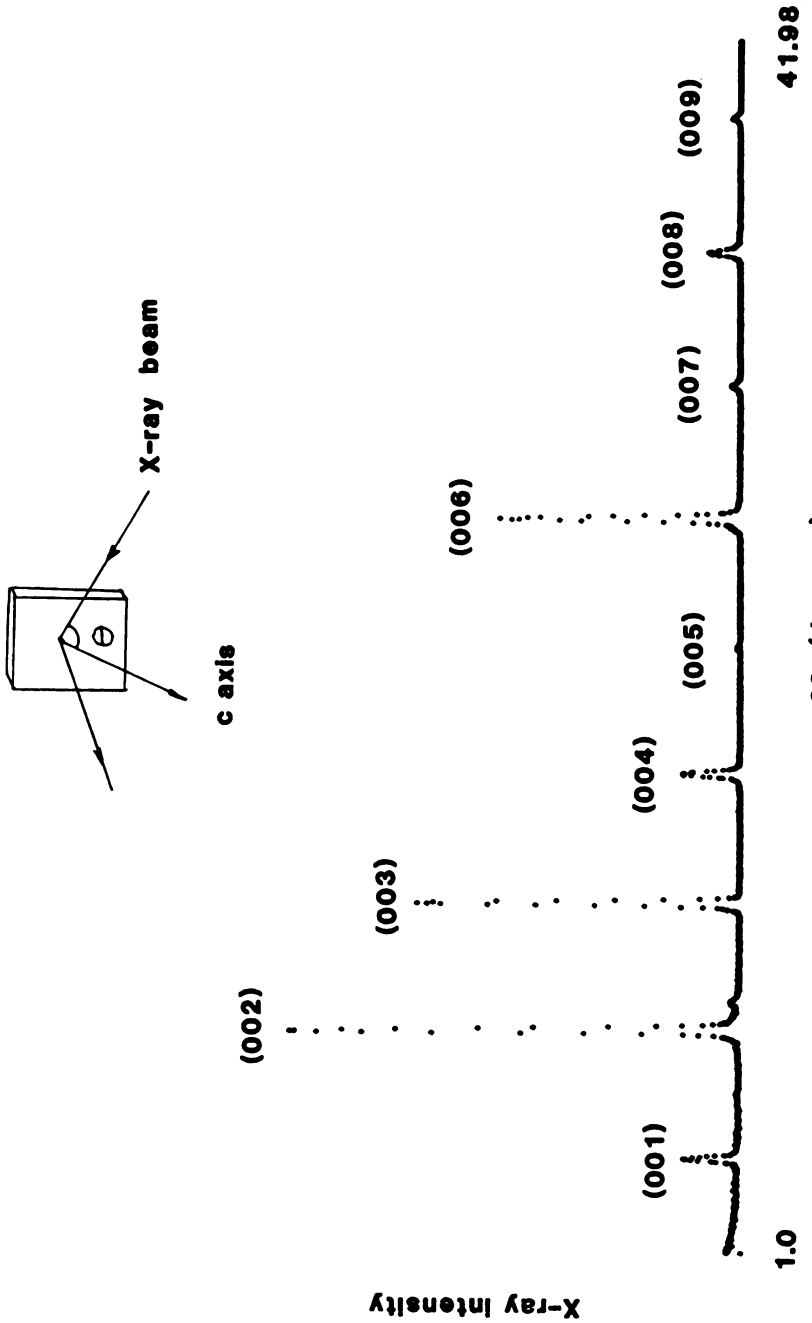

Figure 3.5 00ℓ X-Ray Diffraction Scan, Stage 1 $SbCl_5$.

λ = x-ray beam wavelength.

From this equation, $I_c = S\lambda/2$ where S is the slope from a graph of 00ℓ versus sin θ as measured by the 00ℓ diffraction scan (Figure 3.5). The repeat distances calculated from our characterizations agree with literature values for this compound, and are given in Table 3.1. However, for higher stages ($n \gtrsim 6$) the 00ℓ peaks become closely spaced in 2θ and the stage characterization by x-ray diffraction becomes more difficult. The c-axis mosaic spread is measured by setting the x-ray diffractometer θ and 2θ values to a 00ℓ reflection and then rotating the sample in the x-ray beam (Figure 3.6). Typical mosaic spreads for these compounds ranged from 3 to .6°. The x-ray diffraction measurements were performed with a 12 kW rotating anode x-ray source with a four circle diffractometer and multichannel analyzer. The x-ray beam source target was Molybdenum, and the beam was monochromated to the Kα lines, $\bar{\lambda}$ = .7107A. The resolution of this system in 2θ is about .2°.

The stage 1, 6, and 8 samples loaned to us by the University of Michigan group had been analyzed for their in-plane structure. Their studies indicate the presence at room temperature of the intercalant superlattice shown in Figure 3.3. According to their observations, this $\sqrt{7} \times \sqrt{7}$ superlattice persists to liquid helium temperatures, but below 220K an additional intercalant superlattice appears.[17,20] The new phase was found to be slightly incommensurate with the HOPG lattice, with a unit cell about $\sqrt{39} \times \sqrt{39}$.[17] A group at MIT studying $SbCl_5$ compounds also observed a structural transition near 220K, but their measurements indicate a low temperature in-plane phase without long-range order (glass-like).[21] The c-axis stacking sequence for carbon layers in $SbCl_5$ GIC's is discussed in reference 17.

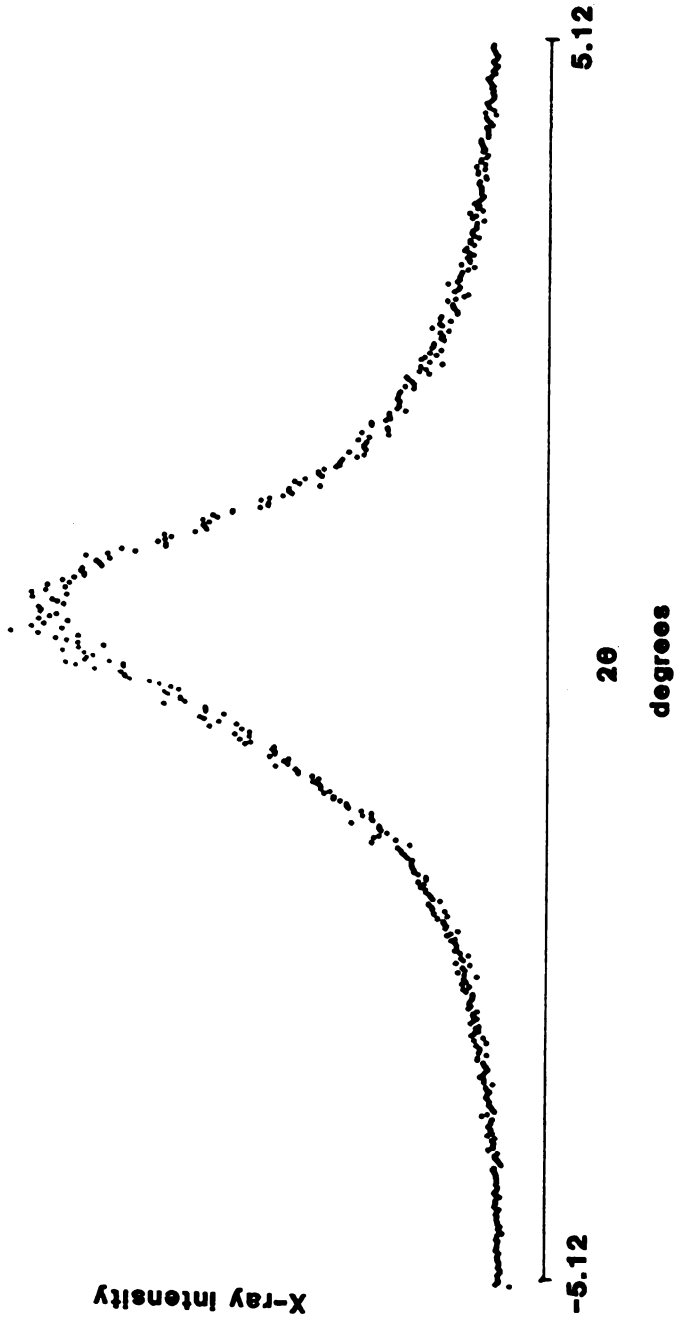

Figure 3.6 Stage 1 Mosaic Spread. Data from the 002 line of Figure 3.5.

The intercalation chemistry for group V pentahalide-graphite compounds such as $SbCl_5$ GIC's remains controversial. The following proposed chemistry has received some quantative support from Mossbauer[22] and x-ray absorption edge spectroscopy,[23]

$$3\ SbCl_5 + 2\ e^- \longrightarrow 2\ SbCl_6^- + SbCl_3\ . \qquad 3.3$$

This, however, has not been confirmed by other techniques.[22] The bulk charge transfer coefficient, f, depends on the number of bonding intercalants, for example the $SbCl_6^-$ molecules in Equation 3.3. The true intercalation chemistry for the $SbCl_5$ GIC's must be determined before accurate calculations of the charge transfer coefficient can be made.

Surface studies were performed on stages 2, 4, and 5 using Raman light scattering and infrared reflectivity techniques. These measurements were used to verify the stage index, independent of the bulk measurements using x-ray diffraction. In all cases, results of the surface and bulk studies were in accord and both indicate that $SbCl_5$ GIC's remain stable for at least 14 months.

CHAPTER FOUR

GIC BAND STRUCTURE AND FERMI SURFACE MODELS

4.1 Introduction

Experimental Fermi surface data on GIC's became available after 1978.[24] Since then several theoretical models have been proposed to describe the observed results. In this chapter those Fermi surface models appropriate to the $SbCl_5$ graphite intercalation compounds studied will be described.

The two GIC Fermi surface and electronic band structure models discussed in this chapter are fundamentally different in their nature and predictions. Prior to describing these models, both of which are phenomenological, we present the 2D and 3D band structures proposed for graphite upon which the GIC models are based.

4.2 Graphite Band Structure and Fermi Surface

The electronic properties of the GIC host material, graphite, are reasonably well understood[25] and are represented by a phenomenological model referred to as the Slonczewski, Weiss, and McClure model (SWMcC).[26,27,28] This model has been used successfully to explain a variety of experimentally measured properties that depend on the electronic structure near the Fermi energy, E_f.[29,30] The SWMcC model has also been confirmed by more sophisticated band structure models,[31] except for one detail which will not affect our arguments.[32]

The 3-dimensional SWMcC model is based on a k • p expansion in the basal plane and the crystal symmetry appropriate to HOPG.[26] The model describes the k dependence of the conduction π bands arising from the weakly-coupled carbon p_z atomic wave functions at the Brillioun zone edges (see Figure 4.1).

The model may be written in terms of a 4 x 4 hamiltonian for the π bands,

$$\begin{pmatrix} E_1 & 0 & H_{13} & H_{13}^* \\ 0 & E_2 & H_{23} & -H_{23}^* \\ H_{13}^* & H_{23}^* & E_3 & H_{33} \\ H_{13} & -H_{23} & H_{33}^* & E_3 \end{pmatrix} \qquad 4.1$$

The H_{ij} are the interaction terms identified with the overlap and transfer integrals between atoms, within the framework of the tight binding approximation, and the E_i are the band edge energies. The interaction terms are,

$$\begin{aligned} H_{13} &= 2^{-1/2}(-\gamma_0 + \gamma_4\Gamma)\,\sigma\, e^{i\alpha} \\ H_{23} &= 2^{-1/2}(\gamma_0 + \gamma_4\Gamma)\,\sigma\, e^{i\alpha} \\ H_{33} &= \gamma_3\,\Gamma\,\sigma\, e^{i\alpha} \end{aligned} \qquad 4.2$$

where α is the angle between k and the Γ K direction, and

$$\Gamma = 2\cos\pi\xi \quad ; \quad \xi = k_z c_0/\pi$$
$$\sigma = \tfrac{1}{2}\sqrt{3}\, a_0 K.$$

The SWMcC band parameters (γ_0-- γ_5, Δ) are given in Table 4.1, a_0 = 1.42Å is the in-plane nearest neighbor distance, c_0 = 3.35 Å is the nearest neighbor distance along the c axis, and K is the magnitude of

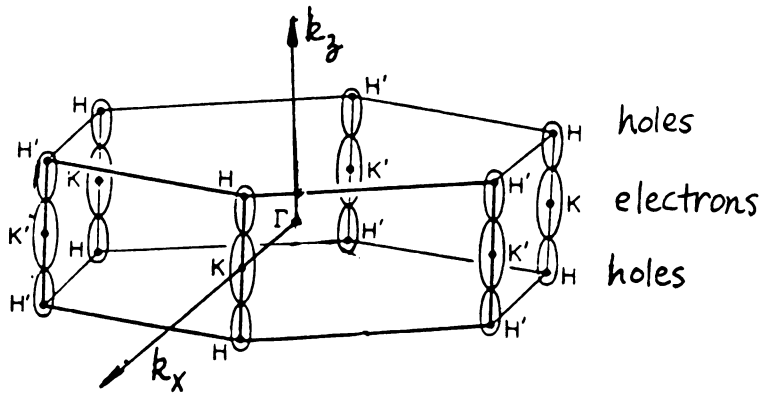

Figure 4.1 Graphite Brillioun Zone and FS.

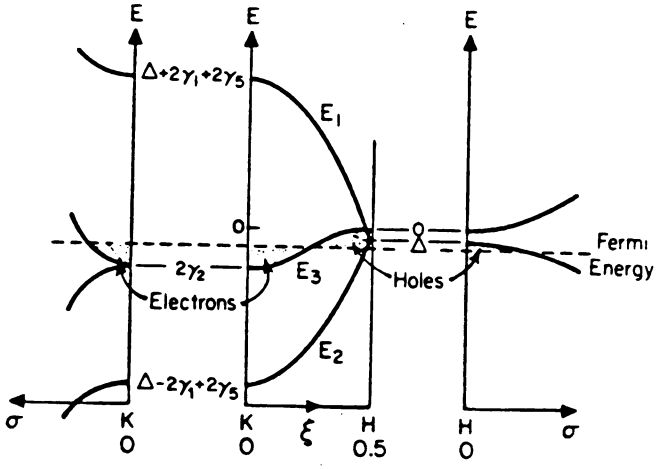

Figure 4.2 SWMcC 3D Graphite Band Structure.

Table 4.1

Slonczewski-Weiss-McClure Band Parameters for Graphite.[13]

Band Parameter	Approximate Value (eV)	Description
γ_0	3.16	Overlap of neighboring atoms in a single layer plane.
γ_1	0.39	Overlap of orbitals associated with carbon atoms located one above the other in adjacent layers.
γ_2	-0.020	Interactions between atoms in next nearest layers and coupling between π and σ bands.
γ_3	0.315	Coupling of the two E_3 bands by a momentum matrix element. γ_3 determines trigonal warping.
γ_4	0.044	Coupling of E_3 bands to E_1 and E_2 bands.
γ_5	0.038	Interactions between second nearest layer planes.
Δ	-0.008	Difference in crystalline fields experienced by inequivalent carbon sites in layer planes.
E_f	-0.024	Fermi level measured from H-point extremum.

the wave vector in the k_x, k_y plane measured from the zone edge. The solutions to 4.1 are

$$E = \tfrac{1}{2}(E_1 + E_2) \pm [\tfrac{1}{4}(E_1 - E_3)^2 + (\gamma_0 - \gamma_4\Gamma)^2\sigma^2]^{\frac{1}{2}}$$
$$E = \tfrac{1}{2}(E_2 + E_3) \pm [\tfrac{1}{2}(E_2 - E_3)^2 + (\gamma_0 + \gamma_4\Gamma)^2\sigma^2]^{\frac{1}{2}} \qquad 4.3$$

where,

$$E_1 = \Delta + \gamma_1\Gamma + \tfrac{1}{2}\gamma_5\Gamma^2$$
$$E_2 = \Delta - \gamma_1\Gamma + \tfrac{1}{2}\gamma_5\Gamma^2$$
$$E_3 = \tfrac{1}{2}\gamma_2\Gamma^2$$

The dispersion relations along the k_z axis given by equations 4.3 are shown in Fig. 4.2. The majority hole and electron pockets found in graphite can be seen to arise from the narrow E_3 band. Fig. 4.1 shows the Fermi surface which results from the SWMcC band structure model. Due to the small extent to which the Fermi surface extends into the k_x, k_y plane, the carrier concentration in graphite is quite low, $\sim 10^{-4}$ carriers/atom, and thus graphite is a classified as a semi-metal. The SWMcC model as described above is used in a rigid band model to be presented in section 4.3.1.

Due to the large observed anisotropy in graphite's transport properties, several 2D band structure models have been proposed.[33,34] These 2D models for graphite have been used as a basis for a 2D band structure for GIC's (Section 4.3.2). Theoretical arguments similar to those used in obtaining the 3D band structure results shown above can be used to obtain the 2D graphite band structure. The 2D hamiltonian is 2 x 2 with solutions,

$$E_{c,v} = \pm \frac{3}{2}\gamma_0 b k \qquad 4.4$$

where c,v refer to the conduction and valence bands, b is the nearest neighbor in-plane carbon-carbon distance, 1.42 Å and γ_0 is the resonance integral between nearest neighbor carbon atoms with a value of $\sim$ 2.4eV.[35] The momentum vector k is measured from the zone edges H and H'(see Figure 4.1) of the carbon Brillioun zone. The simple linear dispersion relation given by Equation 4.4 is not shown.

4.3 GIC Band Structure and Fermi Surface Models

The graphite band structure models above have been used as a basis for a theoretical description of the electronic structure of GIC's. The first theory to be considered views GIC's as modified 3D graphite with a new c-axis periodicity and an increased carrier concentration. The second theory views GIC's as modified 2D graphite and has a strong dependence on intercalant in-plane order.

4.3.1 The Rigid Band Models

In the case of dilute graphite intercalation compounds one might expect the GIC electronic band structure to closely resemble that of graphite. This is the basis of the rigid band model.[36] In it we assume that the GIC band structure is identical to graphite, as represented by the SWMcC model, and allow the Fermi level to shift, so as to accomodate the additional electrons (donor GIC's) or holes (acceptor GIC's) from the intercalant. For typical shifts of the Fermi level, ($>2\gamma_5$) the new carrier pockets will extend from ξ = -.5 to .5, and also extend farther into the k_x, k_y plane. For donor compounds the carrier pockets will be electron-like, and for acceptors only holes are found in the Brillioun zone. Although this model was originally intended for dilute, i.e.

$n \gtrsim 4$ compounds,[36] it has been used to describe the band structure of compounds as concentrated as stage 2.[37,38] In presenting this model we shall consider only the case of acceptor compounds, where the Fermi level shift is towards increasingly negative energy values.

The carrier pockets arise only from the E_3 band. By solving Equations 4.3 we find the following analytic expression for the cross sectional area of the hole pockets formed along k_z (see Figure 4.3):

$$A_h\,(k_z,\, E_F) = \frac{4\pi}{3a_0^2\gamma_0^2}\,\frac{1}{(1-\nu)^2}\,(E_1 - E_F)\,(E_3 - E_F) \qquad 4.5$$

$$\nu \equiv (\gamma_4/\gamma_0)\,\Gamma\,.$$

We now have an expression which gives the size and shape of the new GIC Fermi surface as a function of the Fermi level shift, which is related to the concentration of intercalant present in the sample.

A significant improvement can be made to the rigid band model by including the new c axis periodicity due to staging.[37] The hole cross section as a function of k_z and E_f is still given by Equation 4.5, but it is in a new Brillioun zone. Fermi surface measurement techniques, such as MTO, measure the extremal cross sectional areas of the carrier pockets. To predict these cross sections from the rigid band model we evaluate A_h at points along k_z corresponding to the zone center and new zone edges. Thus, the Fermi surface is cut at points along k_z given by

$$\xi = \tfrac{1}{2}\,(I_c^0/I_c)\;i \qquad i = 0,\, 1,\, 2,\, 3,\, \ldots\, m \qquad 4.6$$

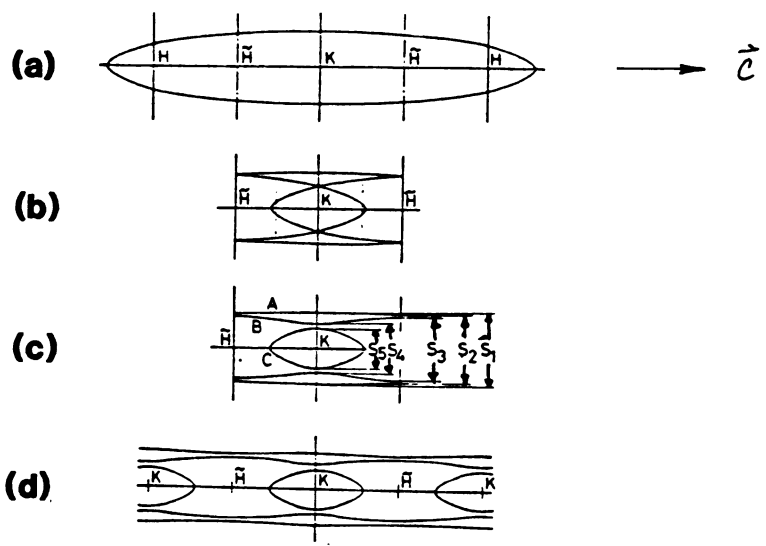

Figure 4.3 Schematic of RBM FS.

(a) RBM FS cross section.

(b) FS shown folded back into the new Brillioun zone.

(c) FS segments from (b) including crystal field effects.

(d) FS segments shown in the extended zone scheme.

where I_c° is 6.70Å and I_c is the c-axis repeat distance for the given stage index. For a fixed stage, we make a total of m cuts along the Fermi surface, each of which corresponds to an extremal cross section. The smallest orbit is given by i = m. A schematic representation of this method is given in Figure 4.3.[38] To apply the rigid band model in predicting the GIC Fermi surface, the largest Fermi surface orbit is used as a parameter in the theory. E_f is adjusted by requiring a match between the models largest cross section at $\xi = 0$, the K point, and the largest Fermi surface orbit. (However, see section 5.3). With the Fermi level fixed, the Fermi surface is given by Equations 4.5 and 4.6.

More recent rigid band theories by Dresselhaus et al.[39-41] differ somewhat in the approach taken, and include another aspect of intercalation, the in-plane order. Briefly, these authors replace the intercalant layer with a vacuum layer and then zone fold along k_z, and also in the k_x, k_y plane consistent with the intercalant superlattice. The orbits predicted from this model differ slightly with those from the model described above. It is important to note, however, that the effect of the in-plane zone folding on the predicted orbits is very small and can be ignored in the rigid band approximation.

To summarize, the rigid band model assumes that the band structure remains graphitic and that changes take place only in the size of the carrier pockets and in the Brillioun zone along k_z. Also, by matching the largest Fermi surface orbit with that predicted at $k_z = 0$, the K point, all other orbits are fixed. Thus, this theory has one 'free' parameter. From Equation 4.5, we can find the total carrier density by integrating over k_z, which will be used in determining the bulk charge transfer coefficient. As will be shown in Chapter 5, the effective mass

for each orbit can be calculated from curves of E_f versus orbital area. Finally, we have assumed no distortion of the graphite band structure due to intercalation. Intuitively this assumption will fail for compounds with a high concentration of accepted (or donated) carriers. The limit of validity might be expressed as a maximum Fermi energy shift, and a likely value is $\sim$ .8 eV. [42]

4.3.2 The 2D Band Structure Models

The electronic band structure and Fermi surface models in this section are two dimensional, and have a strong dependence on the in-plane ordering of the intercalant. First to be described is a model proposed for dilute compounds, and then models intended for the more concentrated compounds, i.e. stages 1-4.

The model for high stage compounds (n > 4) consists of the following features.[24,43] Along the c-axis we find regions of pure 3D graphite, separated by graphite-intercalant-graphite packets. Each of these components will have a unique electronic structure. From section 4.1 we already understand the 3D graphite electronic band structure and Fermi surface. The other component is a metallic sandwich formed by the intercalant and its bounding graphite layers, and has an electronic structure dependent on the intercalant superlattice and the charge transfer. The in-plane superlattice of the intercalant will introduce a new periodic potential in the now highly charged bounding graphite planes. As a result, a new Brillioun zone is formed in the k_x, k_y plane due to the intercalant. This Brillioun zone is used with a nearly-free electron model in the Harrison method[44] to construct the 2D Fermi surface of the metallic sandwich. The Fermi circle is given by the quadratic free-electron dispersion relation, and by,

$$\frac{fN}{2} S_{BZ} = A_{FS} = \pi k_F^2 \qquad 4.7$$

where fN is the number of "free" charge carriers per primitive cell, S_{BZ} is the area of the new in-plane Brillioun zone, and A_{FS} is the area of the Fermi surface. The factor of 1/2 accounts for the charge being distributed equally between the two graphite layers bounding the intercalant. An example of a Fermi surface constructed in this manner is shown in Figure 5.7.

There are several important aspects of this model. First, because we have used a 2D construction for the metallic sandwich, its Fermi surface must be cylindrical, that is, independent of k_z. Second, as mentioned above, the dilute GIC in this model is assumed to consist of two separate components, one being 3D graphite and the other a metallic sandwich. Thus, we should observe two Fermi surfaces in dilute GIC's, one due to 3D graphite as described in section 4.2, the other a new 2D Fermi surface arising from the graphite-intercalant-graphite packets. Finally, this model has no explicit stage dependence except for small variations in the charge transfer coefficient as a function of stage. Thus, to first order, the Fermi surfaces in this model are stage independent, assuming the intercalant in-plane order does not depend on stage.

The 2D band structure and Fermi surface models for stages 1-4 are based on the band structure of 2D graphite, as opposed to assuming the nearly free-electron band structure used for dilute GIC's.[35] The low stage compounds are viewed as follows. The charge transfer gives rise to localized carriers in the intercalant layers and delocalized carriers in the neighboring graphite layers. The localized carriers in the intercalant layers form a high potential barrier preventing carrier

movement along the c-axis. This barrier isolates the highly-charged, graphite-like layers between intercalant layers which are then modeled as 2D electronic subsystems. The sample consists of sequences of these subsystems.

For stage 1 compounds, with one graphite layer between intercalant layers, the 2D band structure for graphite presented in section 4.2 is used as is (see Equation 4.4). The Fermi momentum k_f is calculated in this model from

$$k_F = \sqrt{\pi n} \qquad 4.8$$

where n is the number of holes per unit surface of the GIC. With k_f known, E_f may be determined from Equation 4.4. The Fermi surface is constructed by centering isoenergy circles of radius k_f at corners of the Brillioun zone generated by the intercalant superlattice, see Figure 5.6. The reduced zone scheme is then used to find the k space orbits in the k_x, k_y plane. In predicting orbits from this model, one of the experimentally observed orbits is matched with an orbit constructed by varying k_f of the circles used in the Brillioun zone. Once k_f is found, other orbits are predicted, and E_f, the carrier density, and the charge transfer coefficient are fixed by Equations 4.4 and 4.8.

For stage 2 compounds there are two graphite-like layers between intercalant layers. The graphite layers interact, modifying the single layer band structure in Equation 4.4. Without presenting details, the new band structure is

$$E_{c_1} = -E_{v_1} = \tfrac{1}{2}[(\gamma_1^2 + 9\gamma_0^2 b^2k^2)^{1/2} - \gamma_1] \qquad 4.9$$

$$E_{c_2} = -E_{v_2} = \tfrac{1}{2}[(\gamma_1^2 + 9\gamma_0^2 b^2k^2)^{1/2} + \gamma_1]$$

where the new parameter γ_1 is the resonance integral between nearest carbon atoms in the two graphite layers, and depends on the charge transfer coefficient.[35] It is assumed[35] that the value of γ_1 in GIC's is the same as that for pure graphite. In stage 2 compounds two values are found for k_f. The Fermi surface is constructed by centering two isoenergy surfaces of radius k_{f1} and k_{f2} at the corners of the intercalant Brillioun zone then zone folding in the k_x, k_y plane. The values of k_{f1} and k_{f2} are fixed by requiring agreement with two or more of the Fermi surface cross sections. The Fermi energy, additional predicted cross sections, and the charge transfer coefficient are then fixed. Expressions relating k_{f1} and k_{f2} to E_f, carrier densities, and the charge transfer coefficient can be found in references 35 and 46.

For GIC's of stage 3 and 4, not all of the graphite layers between intercalant planes are equivalent.[45] In a stage 3 compound, the additional graphite layer is in a new environment, being bounded on either side by highly-charged graphite layers. This requires a variable charge density in the graphite packet between the intercalant layers, and the resultant band structure is complex. Attempts to apply the 2D model to stage 3 and 4 GIC's have not been very successful[45] and will not be used in analysis of our experimental results.

The 2D models presented are summarized by the following. For dilute compounds, two electronic structures are present; one corresponding to 3D graphite, the other corresponding to a 2D metallic sandwich resulting from, and depending on the intercalant superlattice. For low stage compounds, the Fermi surface is strictly 2D and again dependent on the in-plane intercalant superlattice.

4.4 Comments

There are several effects not accounted for by the RBM and the 2D model, and also not included in the working expression for MTO, Equation 1.14. These effects are observable in certain materials. The first effect, called the B-H effect, was first included in the theory of the dHvA effect by Shoenberg.[47] A quasiparticle sees not just the applied magnetic field $\vec{H}$, but the flux density $\vec{B}$. A calculation by Gold[48] shows that this effect causes additional, non-harmonic frequencies to arise. Given fundamental frequencies F_a and F_b, this effect will create lower amplitude orbits such as $2F_a$, $2F_b$, $F_a + F_b$, $F_a - F_b$, etc. The second effect which can also couple fundamental frequencies is called magnetic breakdown (MBD) and was first included in the theory of the dHvA effect by Falicov and Cohen.[49] Magnetic breakdown arises when the magnetic potential is sufficient to cause interband transitions which then couple one semi-classical quasiparticle orbit to another, resulting in sum or difference frequencies, $F_a - F_b$, $F_a + F_b$. The above effects are discussed in reference 9. A third mechanism by which fundamental orbits may be coupled is charge density waves (CDW). New orbits can be obtained by superposing FS "saddle points" through a CDW translation vector resulting in sums and differences of fundamental FS orbits, see references43, 50, 51. Finally, crystal field effects which would cause gaps to appear at zone edges (Figure 4.3(c)) will result in entirely new cross sections of the FS, see reference 52.

CHAPTER FIVE

EXPERIMENTAL RESULTS AND ANALYSIS

5.1 Introduction

Fermi surface data from our experiments is given in section 5.2. In 5.2.1, we present measurements on the graphite host material HOPG, and 5.2.2 through 5.2.7 cover the results for the $SbCl_5$ compounds. A general discussion of the data follows this presentation. In section 5.4 the two GIC Fermi surface models of Chapter 4 are applied to our results. We finish the chapter with our conclusions.

5.2 Fermi Surface Results

Before presenting our data, we make some introductory comments on the nature of our data presentation and the scope of this study.

Results of Fermi surface (FS) studies on graphite acceptor compounds performed by other groups,[43,46,52,53] as well as this study, indicate a large number of deHaas-van Alphen (dHvA) frequencies present in these compounds. The largest frequency is typically more than an order of magnitude higher than the smallest. Usually, the frequency spectrum will also contain several closely spaced frequencies (i.e. a few percent apart). The data set for each sample studied consists of several dozen frequency scans, each covering a different range of dHvA frequencies. This is done to improve the signal-to-noise ratio for

Table 5.1

Experimental Results on HOPG and $SbCl_5$ Compounds

(Frequencies in MG)

Uncertainties are typically <2%

HOPG	STAGE 1	STAGE 2	STAGE 4	~STAGE 6	~STAGE 8
		(13.7)			
.0670	12.3	9.5	7.05	6.5	?
				5.35	
.0496	11.4	7.5	6.80	4.46	2.50
.0061*	10.5	6.6	6.60	2.24	2.11
	3.2	6.0	6.38	1.50	1.55
		3.68	3.20	1.24	1.08
		3.10	2.06	1.00	1.00
		2.50	1.72	.84	.38
		1.54	1.58	.46	.32
		.96	1.32	.41	.24
		.56	.84	.38	.23
			.42	.23	.15
					.10
					.075

*Uncertainty ~13%.

selected orbits, or groups of orbits. However, for the sake of brevity, only one scan which covers the entire frequency range appropriate to that compound will be presented. The cumulative results from all scans for each compound are listed in Table 5.1.

The primary focus of this research is to characterize the size and shape of the FS for each compound of a given stage. However, the MTO technique can also be used to obtain information on the effective mass and Dingle temperature for each observed orbit. Recall from Chapter One that the MTO amplitude dependence on the effective mass is somewhat weak, and therefore this technique is not well suited for effective mass measurements. Attempts at determining the effective mass for these compounds have been somewhat unsatisfactory. This is due partly to the above reason, but primarily due to the difficulty in separating closely-spaced frequencies, which is required for an accurate measurement of the amplitude of a given dHvA frequency. The effective mass must also be known to determine the Dingle temperature (Equation 1.18). The effective mass and Dingle temperature is obtained for the lowest frequency orbit of a stage 6 compound, in section 5.2.5, as an example of the method of measurement of these parameters using MTO.

5.2.1 HOPG

FS measurements were performed on the graphite host material, HOPG. These studies, performed at about .9K, confirmed the quality of the host material and also served as a test of the experimental technique. The dHvA frequencies observed are listed in Table 5.1, for the c-axis parallel to the magnetic field direction. These frequencies are in excellent agreement with the results of Shubnikov-deHaas[30] and

deHaas-van Alphen[29] measurements, and also confirm the SWMcC FS model described in section 4.2. The agreement of the frequencies given by our transforms and these earlier results also indicate that the cryostat, magnetic field calibration, and the computerized acquisition and analysis techniques are satisfactory.

5.2.2 Stage 1 $SbCl_5$

Experimental FS results on a small (5mg) stage 1 sample provided by R. Clarke, University of Michigan, are shown in Figure 5.1(a). The small sample size resulted in a small MTO amplitude due to thermal loading by the support and sensor. Because of this, and the additional decrease in amplitude with angle (section 5.3), studies of the rotation dependence of the dHvA frequencies could not be performed. The four frequencies obtained for c ∥ H are listed in Table 5.1. Structural studies by x-ray analysis indicated a small (~ 5%) admixture of stage 2 in this compound. However, none of the frequencies associated with stage 2 compounds, from section 5.2.3, were observed in this sample. Note that the typical stage 1 dHvA frequencies are at least two orders of magnitudes larger than those found in HOPG.

5.2.3 Stage 2 $SbCl_5$

Three stage 2 compounds were investigated. Two of the compounds were produced locally, the third was provided by the University of Michigan group. The dHvA frequencies obtained on all three samples are in agreement, and are listed in Table 5.1. A representative scan for stage 2 compounds appears in Figure 5.1(b).

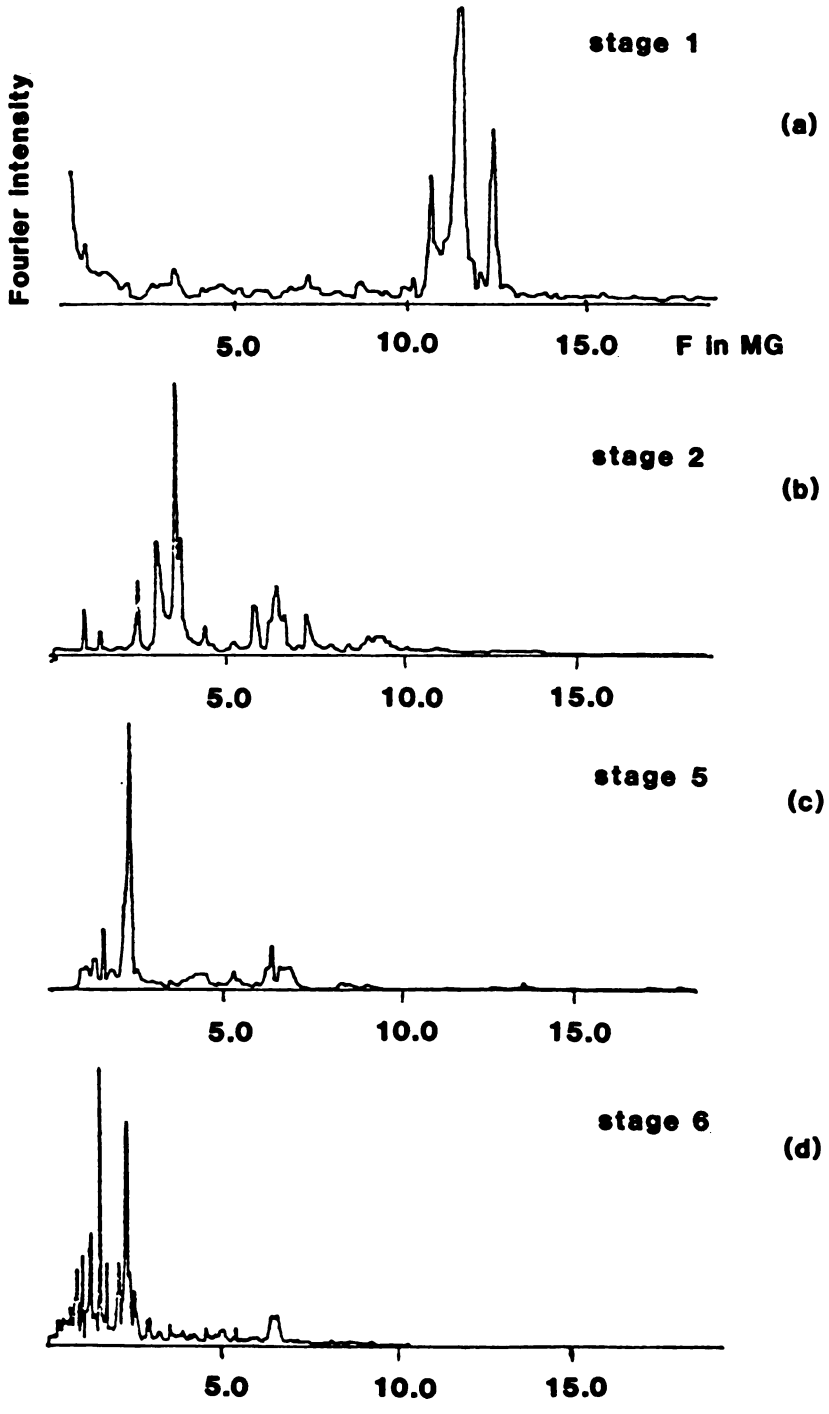

Figure 5.1 Stage Dependence of $SbCl_5$ FS.
All data taken at T∿.9K with c||H.

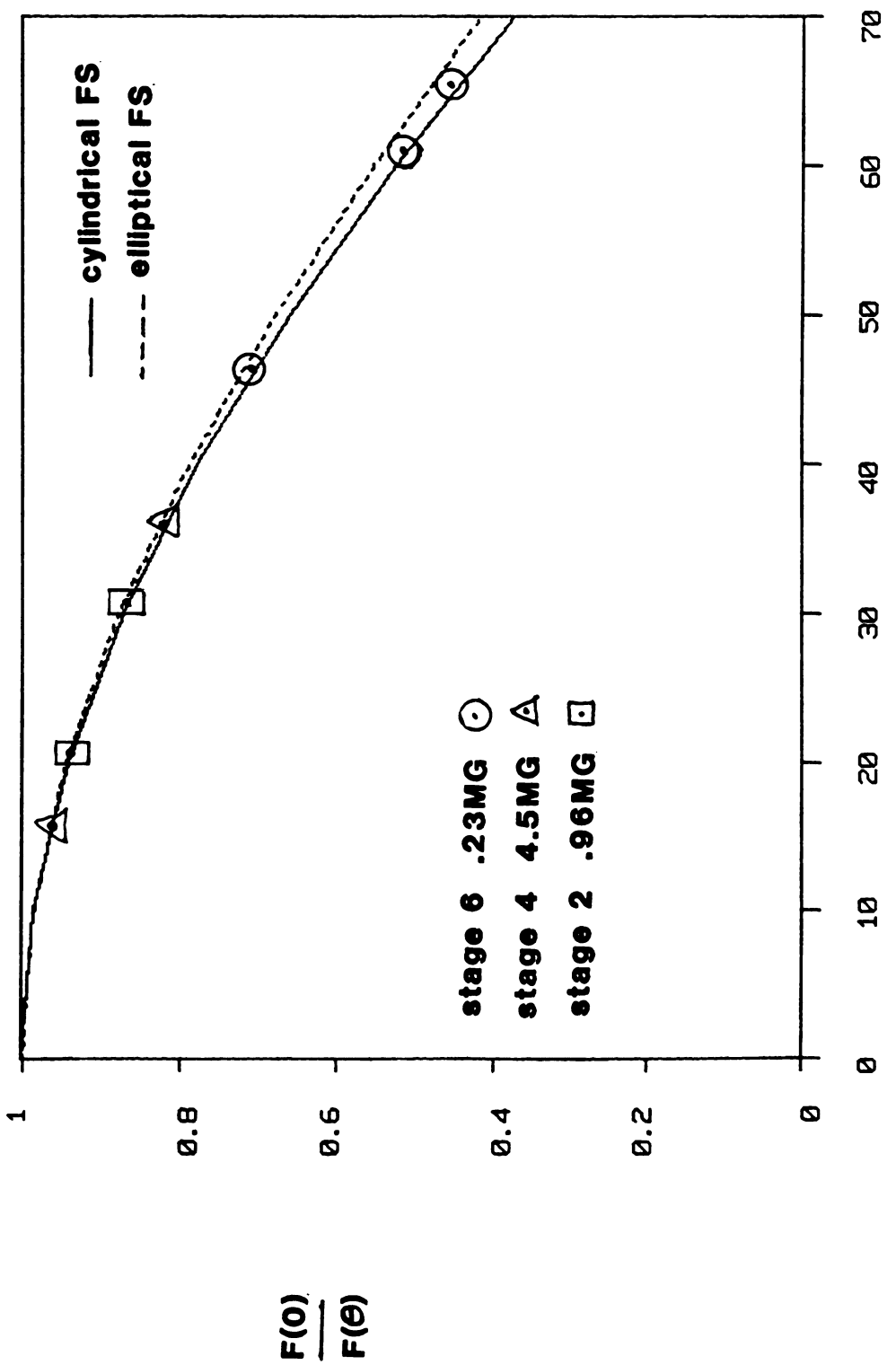

Figure 5.2 Rotation Dependence of dHvA Frequencies.

Studies of the rotation dependent shift of the dHvA frequencies, which yield geometrical information, were performed for angles up to 40° for several orbits. In Figure 5.2 we display, for the sake of clarity, only a few representative datum points for the .96 MG orbit of the stage 2 compounds. In that figure we also show some of the results for stage 4 and stage 6 compounds. The rotation data obtained for different orbits within a given stage, and for different stages, all indicate the same type of angular dependence. Two theoretical curves are also shown in Figure 5.2. One curve indicates the rotation dependence predicted for a cylindrical FS, the other for an ellipsoidal FS, see section 5.4.1. We will interpret the rotation data in section 5.4.

5.2.4 Stage 4 $SbCl_5$

The dHvA frequencies obtained for a locally produced stage 4 compound are given in Table 5.1. Rotation studies were performed to 35° and are shown in Figure 5.2. Figure 2.6 is one example of the low frequency scans for stage 4.

5.2.5 Stage 5 $SbCl_5$

Two stage 5 compounds produced locally were studied. Characterization by x-ray analysis indicated a presence of stage 6 in the first sample. The frequencies observed in this mixed stage sample are shown in Table 5.2, along with the frequencies associated with stage 6. We see that many of the frequencies attributed to pure stage 6 are shared by this mixed stage sample. This might indicate that stage mixing in this sample consists of separate macroscopic domains of each stage. The size of these domains has not been ascertained. Typical data obtained

Table 5.2

Sharing of Frequencies in a Mixed Stage 5 and 6 Compound

Stage 5 & 6	Stage 6
6.92*	
6.5	6.5
5.4	5.35
	4.46
4.3*	
2.25	2.24
2.04*	
1.73*	
1.50	1.50
1.25	1.24
1.00	1.00
.89*	
	.84
	.46
	.41
	.38
.23	.23
.14†	

*Indicates frequencies attributed to stage 5 and confirmed by the other stage 5 compound.

†This frequency found in stage 8.

on this sample is shown in Figure 5.1(c). Rotation studies (not shown) were also performed on this sample. Analysis of the data yields the same behavior as seen in Figure 5.2 for the other stage compounds. The second stage 5 sample cleaved during preparation and consequently gave poor FS data. However, this sample did confirm the stage 5 frequencies indicated in Table 5.2.

5.2.6 Stage 6 $SbCl_5$

The stage 6 compound studied was produced by the University of Michigan group. X-ray diffraction characterization indicated stage 6 for this sample, but stage analysis generally becomes more difficult with increasing stage index ($n \gtrsim 6$), as mentioned in section 3.4. In addition, one is likely to form mixed stage compounds during synthesis for stages 6 and higher.

The dHvA frequencies obtained for the nominally stage 6 compound are listed in Table 5.1, and a typical frequency scan is shown in Figure 5.1(d). The rotation dependence of the lowest frequency orbit, for angles up to 65°, is shown in Figure 5.2.

Studies of the temperature dependence of the MTO amplitude for fields between 3.4 and 20 kG were performed for the lowest frequency orbit, .23 MG. As described in section 1.3.3, analysis of the temperature dependence of the MTO amplitude A_i for a given magnetic field value will give the effective mass. In Figure 5.3, we have shown the measured MTO amplitude ratio as a function of temperature for H_0 = 15kG. Also shown in that figure are amplitude ratio curves generated from Equation 1.17 for H_0 = 15kG, and m_c^*/m_0 values ranging from .2 to .4. A good fit to the experimental data is obtained for m_c^*/m_0 = .285. Given this value

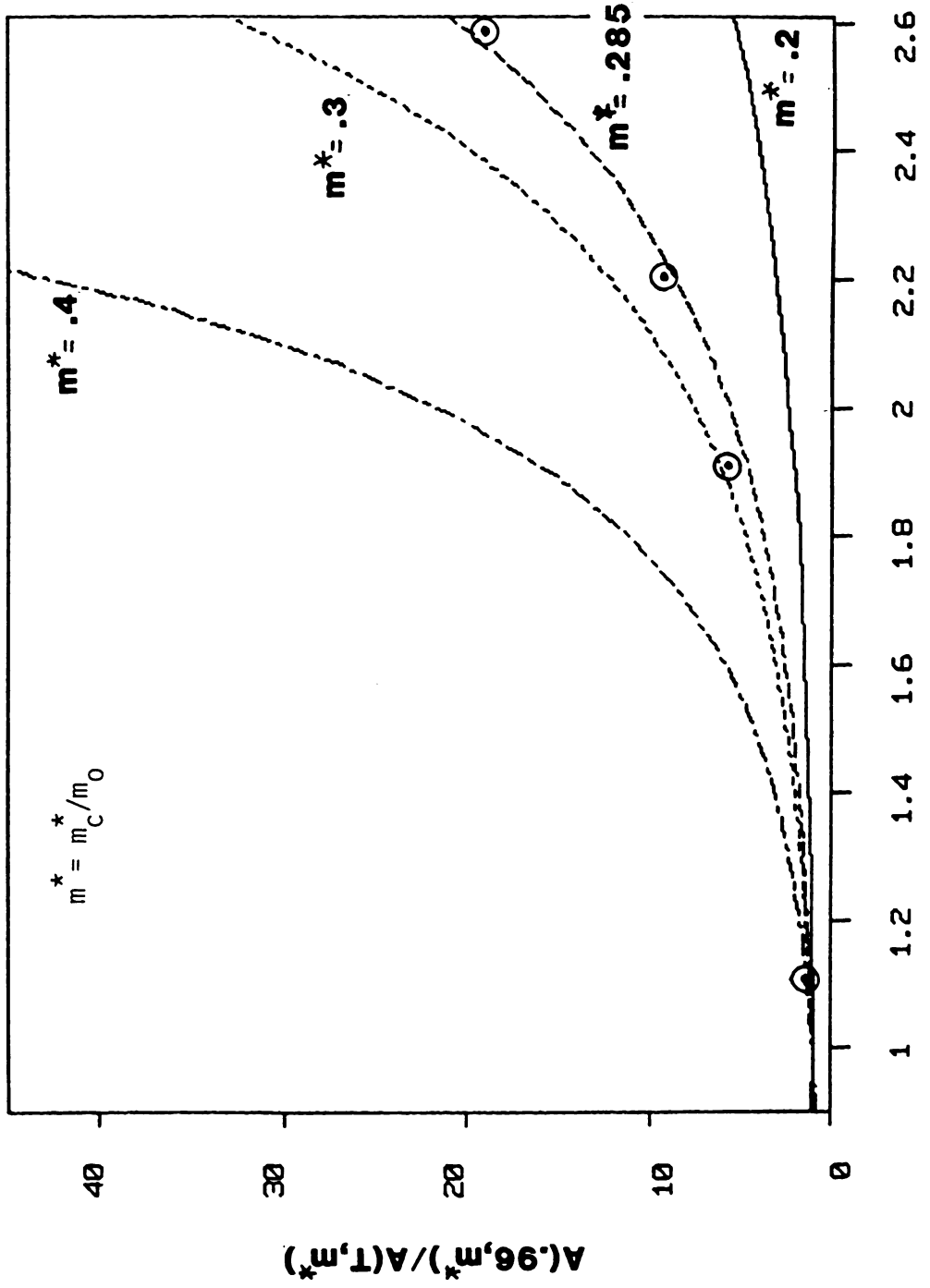

Figure 5.3 MTO Amplitude verses Temperature.
.23MG orbit, Stage 6

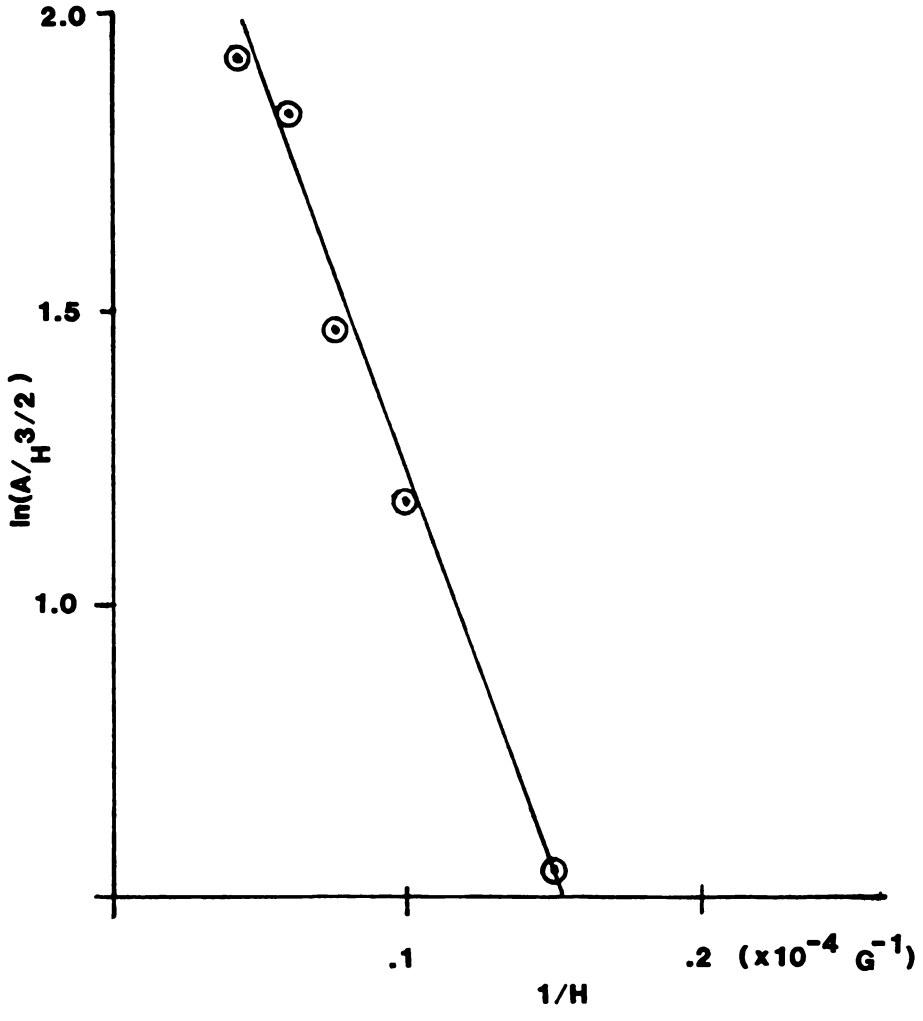

Figure 5.4 MTO Amplitude verses 1/H.
.23MG orbit, Stage 6

for the effective mass, T_i, the Dingle temperature, may be obtained from the field dependence of the MTO amplitude at fixed temperature from a plot of $\ell n(A_i/H^{3/2})$ vs. 1/H, as shown in Figure 5.4. The slope of the line generated gives the Dingle temperature from Equation 1.20. From this data the Dingle temperature for the .23 MG orbit is found to be 2.5K.

5.2.7 Stage 8 $SbCl_5$

Results on a nominally stage 8 compound, also produced by the University of Michigan group, are given in Table 5.1. General features of the frequency spectrum are similar to those shown in Figure 5.1(d) for stage 6, and hence the stage 8 scan is not shown. Considerable time and effort was spent searching for low dHvA frequencies, corresponding to those of graphite on stages 6 and 8, with null results.

5.3 General Observations and Discussion

The relation between the structure and concentration (staging), and the resultant Fermi surface cross sections (dHvA frequencies), is indicated by Figure 5.1 and listed in Table 5.1. One notes a monotonic decrease in the observed frequencies as the stage index is increased. The normalized rotation dependence of the dHvA frequencies is independent of stage and is shown in Figure 5.2.

In reviewing the stage dependent dHvA frequencies observed, there are several features worthy of note. First, we see strong evidence of frequency sharing for different high stage compounds such as stages 6 and 8. For high stage compounds it is difficult to produce good stage fidelity, and from these results it appears that the different stages within a mixed stage compound are separated.

Within a given pure stage compound, it appears that certain frequencies are arithmetic sums of other frequencies appearing in that compound. For example, in stage 2, the 1.54 MG orbit could be a sum of the .56 and .96 MG orbits, indicating magnetic breakdown, or other FS effects discussed in section 4.4. Possible orbit assignments for stage 2 $SbCl_5$ are given in Table 5.3. Earlier results by the dHvA technique on $SbCl_5$ compounds stages 2-4 also provide evidence of arithmetic sums of frequencies, although this was not reported in the article.[53] Also, evidence of magnetic breakdown in MTO experiments on Br,[46] HNO_3,[43] and $SbCl_5$[24] acceptor compounds has been reported. We must also note that sum or difference frequencies could occur from the non-linear nature of our apparatus, in partcular, the MTO sensor, see Equation 2.5. These non-linear effects, however, are too small to be of consequence.

Earlier FS results on stage 2 and 4 $SbCl_5$ compounds using MTO[24] (field modulation technique) and for stages 2, 3, and 4, using the dHvA technique have been published.[53] The frequencies reported for c ∥ H are listed in Table 5.3, along with our observations. We discuss first the results of the other MTO experiment.

Batallan et al.[24] reported observing stage independent FS results for these compounds. In reviewing their article, it can be seen that the dHvA frequecy resolution of their apparatus is poor and may have obscured any stage dependent frequency shifts.

Results of the dHvA studies on stages 2-4 (Table 5.3) generally show higher frequencies than those observed in this study. This disagreement between dHvA frequencies reported by that group and by others is not limited to these compounds. For example, the results of Tanuma et al. show approximately 10-20% higher dHvA frequencies for K

Table 5.3

Published Results from dHvA and MTO Experiments

and the Present Results on $SbCl_5$

Author	n=2	Orbit Assignment*	n=4
Present Results	(13.7)	$F_8 + F_5$	7.05
	9.5	F_8	6.80
	7.5	F_7	6.60
	6.60	$F_6 + F_1$	6.38
	6.00	F_6	3.20
	3.68	F_5	2.06
	3.10	F_4	1.72
	2.50	F_3	1.58
	1.54	$F_1 + F_2$	1.32
	.96	F_2	.84
	.56	F_1	.42
Tanuma et al.[53]	15.2		8.85
	11.9		7.52
	8.47		6.99
	4.42		2.15
	4.22		1.80
	3.98		1.70
	2.56		1.63
	.862		.481
Batallan et al.[24]	5.35		5.50
	3.32		3.30
	1.91		2.00
	1.43		1.44
	.95		.95
	.475		.475

*Note: The orbits F_2-F_8 appear to be cylindrical, or nearly cylindrical, FS segments. F_1 could be either cylindrical or elliptical (section 5.4.1).

compounds in comparison with SdH studies for the same compounds.[37,42] Thus, the disagreement between our values for the $SbCl_5$ compounds and those of the dHvA studies of Tanuma et al. may be due to a systematic error in their experiment, e.g. magnetic field calibration. In general, their results agree reasonably well with ours if we shift their frequencies down by about 10-15%. We also note that while they required very high magnetic fields (up to 150kG) to observe the highest frequency in stage 2, we apparently can detect it with only 50kG fields. In general, the largest orbits (large dHvA frequencies) are best observed using large magnetic fields. This may indicate that our signal-to-noise ratio is better. From our results, and from the results of the dHvA studies, we believe that this highest orbit in stage 2 is due to magnetic breakdown or other orbit coupling effects, and should not be considered as a fundamental orbit, see section 5.4.1.

We have found experimentally that the MTO amplitude is strongly attenuated as the angle between the crystalline c-axis and the magnetic field increases. The signal amplitude decreases below the noise level for angles above 65°. This is related to the amplitude factor $(\partial^2 E/\partial k_z^2)_{ext}^{1/2}$ in Equation 1.14, and to the angle dependence of m_c^*/m_o which appears in other amplitude factors in that equation.

5.4 Predictions from the Fermi Surface Models

The two FS models we wish to compare with our results are; the rigid band model from section 4.3.1, and the 2D model of section 4.3.2. Following the application and discussion of each model we conclude by comparing these models in terms of their ability to account for the observed FS results.

5.4.1 The Rigid Band Model

The rigid band model (RBM) has been used with some success in predicting and interpreting the GIC electronic properties as measured by SdH[37] and dHvA[38,52,53,55] techniques. The model, as originally conceived,[36] was intended for dilute, i.e. $n > 4$ compounds. However, it has also been applied to compounds as concentrated as stage 2.[37,52,53,55] Comments on the range of validity for the RBM are found in section 4.3.1. To apply this model, the Fermi level shift due to intercalation must be determined. From section 4.3.1 this is accomplished by lowering (for acceptor compounds) the Fermi energy, E_f, until the largest predicted dHvA frequency (Fermi surface cross section at the K point, $k_z = 0$) coincides with the largest observed frequency. We have no guarantee, however, that the largest oberved frequency is, in fact, the largest frequency orbit present in the sample, (section 5.3). Once E_f is fixed, other dHvA frequencies are predicted and compared with the experimental results. This model predicts an ellipsoidal FS which, after zone folding, consists of nearly cylindrical segments, and one small elliptical orbit (Figure 4.3). From geometrical arguments, the dHvA frequency shift predicted for an ellipsoidal Fermi surface segment is given by

$$\frac{F(o)}{F(\theta)} = (\cos^2\theta + \frac{a^2}{b^2}\sin^2\theta)^{1/2} \qquad 5.1$$

where $F(o)$ is the dHvA frequency for $c \parallel H$, $F(\theta)$ is the dHvA frequency at angle θ, and a and b are major and minor axes for the small FS ellipse at the zone center. For a nearly cylindrical FS segment, the normalized dHvA frequency shift should vary according to

$$\frac{F(o)}{F(\theta)} = \cos\theta \ . \qquad 5.2$$

Details of the application of this model are given only for the case of the stage 2 compounds; the procedure is the same for all other stages. The variation of the FS cross sections or frequencies given by the RBM as a function of E_f for stage 2 $SbCl_5$ compounds is shown in Figure 5.5. These curves were generated from Equations 4.5 and 4.6 with appropriate values for I_c. For stage 2, the largest fundamental orbit observed is 9.5 MG which implies a Fermi energy of -.77eV. Although we were able to resolve an orbit at 13.7 MG, we believe that this orbit is not fundamental, and is in fact due to magnetic breakdown or other effects given in section 5.3, and should not be used in determining E_f. Note that the Fermi level shift for stage 2 is near the limit of validity of the rigid band model, see section 4.3.1. Once E_f is fixed, the predicted dHvA frequencies are obtained from the curves labeled ξ_1 - ξ_4 of Figure 5.5. These frequencies, and the frequencies observed for stage 2 are listed in Table 5.4. The carrier concentration $n(E_f)$ can be obtained by calculating the volume within the FS. This is done by integrating Equation 4.5 over the variable k_z with E_f fixed. The carrier concentration calculated for stage 2 is also listed in Table 5.4. From the carrier density, $n(E_f)$, and the number density, N, of intercalant molecules, the charge transfer coefficient, f, may be determined from

$$f = \frac{n(E_f)}{N} \ . \qquad 5.3$$

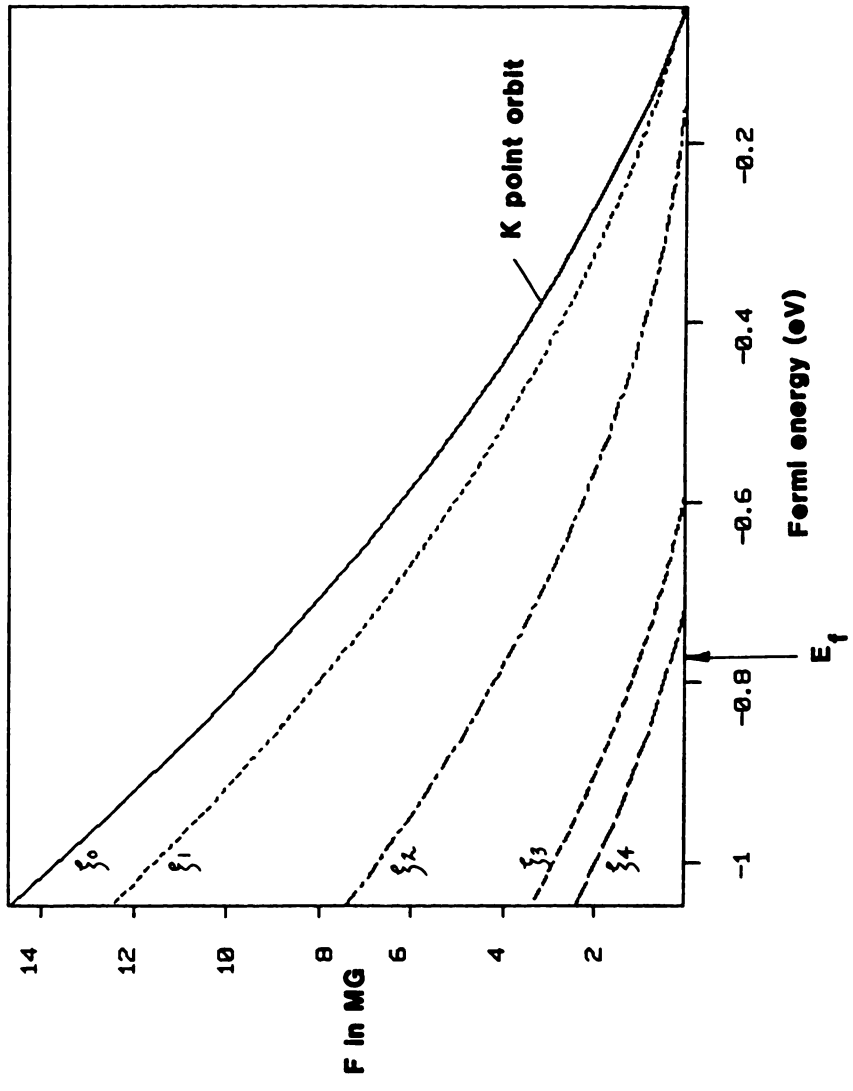

Figure 5.5 RBM dHvA Frequency verses E_f, Stage 2 $SbCl_5$.

Table 5.4

RBM Predictions and Observed Results

$SbCl_5$ Compound	Frequency Observed		Frequency Predicted	E_f(eV)	$n(E_f)cm^{-3}$	f
Stage 2	9.5	F_8	matched	-.77	$1.4x10^{21}$	.65
	7.5	F_7	7.7			
	6.6					
	6.0					
	3.68	F_5	4.0			
	3.10					
	2.50					
	1.54					
	.96	F_2	1.0			
	.56	F_1	.20			
Stage 4	7.05		matched	-.65	$9.2x10^{20}$	.65
	6.80					
	6.60					
	6.38		5.52			
	3.2		4.98			
	2.06		2.82			
	1.72					
	1.58					
	1.32		1.02			
	.84					
	.42					
Stage 5	6.92		matched	-.64	$9.2x10^{20}$	.75
			6.5			
	4.3		5.3			
	2.04		3.6			
	1.73		2.0			
	.89		.61			
Stage 6	6.5		matched	-.58	$7.2x10^{20}$	.69
	5.35		5.66			
	4.46		4.86			
	2.24					
	1.50					
	1.24					
	1.00		1.00			
	.84					
	.46					
	.41					
	.38					
	.23		.12			

For total ionization of $SbCl_5$ molecules, f would be one. In calculating N for the $SbCl_5$ compounds, we have used the accepted $C_{14n}SbCl_5$ stoichiometry, and assumed that all intercalant molecules transfer charge equally. As was discussed at the end of Chapter 3, this assumption may not be justified. However, with this assumption the resultant charge transfer is listed in Table 5.4.

The above procedure was followed for compounds of stage 4, 5, and 6, and the results are given in Table 5.4. Due to difficulties in confirming the largest orbits for stages 8, the model could not be applied to that compounds. It is important to note that the predictions of this model are based on the assumption that we have observed, for each compound, the largest dHvA frequency which is used to determine E_f and upon which all other calculated quantities, $n(E_f)$, and f are based.

The agreement between the observed dHvA frequencies and those predicted by the RBM is only qualitative. This is not surprising in view of the simplicity of this model. From Table 5.4 it is seen that the RBM also underestimates the number of dHvA frequencies to be observed. This is due to at least two causes. First, the RBM as applied does not include crystal field effects and other possible phenomena which would result in several additional orbits, see section 4.4. Effects of the crystal field were estimated by Tanuma et al. in analyzing their results on AsF_5 compounds, see Figure 4.3.[52] Second, some of the experimental frequencies appear to be harmonics of a fundamental and others are possibly due to magnetic breakdown or other effects coupling fundamental orbits, see section 5.3.

Studies of the rotation dependence of the dHvA frequencies on selected orbits in different stage compounds are shown in Figure 5.2.

From the RBM we expect the smallest FS segment to be elliptical, as shown in Figure 4.3. The remaining orbits should display a frequency shift consistent with the angular variation predicted by Equation 5.2 for cylindrical Fermi surfaces. In Figure 5.2, curves generated from Equation 5.1 for b/a = 5, and from 5.2 are shown. The higher frequency orbits shown in that Figure are consistent with a cylindrical Fermi surface geometry, at least to 45°. The smallest of the orbits for the stage 6 compound, .23 MG, was observable only to 65°, where the MTO signal decreased below the noise level. Unfortunately, data to this angle can be interpreted equally well in terms of an ellipse, or as a cylindrical FS segment. Thus, on the basis of the data obtained, the FS consists of cylindrical, or nearly cylindrical, segments aligned along k_z.

We can calculate cyclotron effective masses from the RBM by determining the slopes of the cross section (frequency) curves evaluated at E_f (e.g. Figure 5.5) and using,

$$m_c^* = \frac{h^2}{2\pi} \frac{dA}{\partial E}\bigg|_{E_f} . \qquad 5.4$$

A calculation of m_c^* for the .23 MG orbit of the stage 6 compound gives a RBM value of $m_c^*/m_o \sim .35$ which compares well with the measured value of .3 from section 5.2.6.

The FS data from dHvA and SdH experiments have also been evaluated using the RBM.[37,38,52,53,55] The $SbCl_5$ compounds stages 2, 3, and 4 were studied using the dHvA technique. The published results[53] of that study listed only the charge transfer coefficient calculated from the RBM, which ranged between .43 and .49; in general agreement with our

results. Analysis of low stage K and Rb compounds studied by the SdH method were analyzed using this model.[37] The trend we observe in f increasing for increasing stage (excluding stage 5) was also observed in their results. This implies that the intercalant molecules are more fully ionized for more dilute compounds.

The Fermi energy may be inferred from several other experimental techniques. To date, however, the only technique other than Fermi surface methods, is the study of infrared and visual optical reflectivity. The results of several experiments[35,56,57,59] are shown in Table 5.5 along with the values calculated from our MTO measurements using the RBM. The agreement is in general quite good.

5.4.2 The 2D Model

We now apply the 2D FS model described in section 4.3.2 to our results. This model has been used in interpreting both optical[35] and MTO FS data[24,43,46,58] on several graphite acceptor compounds. We shall present the procedure for our stage 1 compound. The method for constructing the Fermi surfaces for stages 2-4 is similar, although more complex. Following discussion of stages 1-4, we interpret our results on stages 6 and 8 using the dilute limit of the 2D model.

As discussed in section 4.3.2, the intercalant in-plane structure, which determines the Brillioun zone for in-plane zone folding, is of central importance in this model. A discussion of the issue of what superlattice is appropriate to the $SbCl_5$ compounds at low (4K) temperatures is found in section 3.4. The stage 1 compound studied was characterized for in-plane structure by the University of Michigan group. We base our calculation of the $SbCl_5$ GIC Brillioun zone on

Table 5.5

E_f as Determined by MTO and RBM and Values from Other Experiments

Values in (eV)

Source	n=1	n=2	n=3	n=4	n=5	n=6
Present Study	-.94	-.77		-.65	-.64	-.58
Ref. 56 Optical Refl.		-.72	-.62	-.60		
Ref. 35 Optical Refl.		-.75				
Ref. 59* Optical Refl.	-1.2	-.94				
Ref. 57 from Thermopower Data		-.79	-.43		-.3	

*Used adjusted values for band parameters.

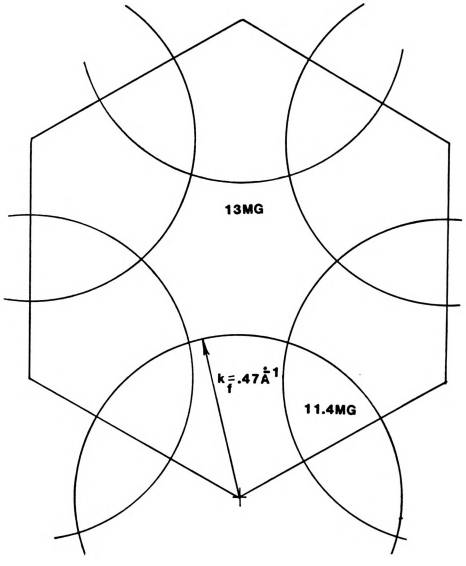

Figure 5.6 2D FS Construction, Stage 1 $SbCl_5$.

the $\sqrt{7}$ x $\sqrt{7}$ superlattice structure discussed in section 3.4, which gives the hexagonal zone shown in Figure 5.6. Assuming this intercalant structure we use the Harrison construction for determining the FS given the appropriate (stage dependent) band structure.

For stage 1, the 2D band structure is given by Equation 4.4. The Harrison construction is used in Figure 5.6 where the 1st Brillioun zone is shown and the isoenergy circles of radius k_f are drawn at the zone corners as prescribed by this model. The value of k_f is adjusted until the zone-folded Fermi surfaces best agree with our observations. The best fit found is shown in that Figure where we have matched the 11.4 MG orbit by adjusting k_f to a value of $.47\text{Å}^{-1}$. A second orbit is then predicted at 13 MG. From this value of k_f and Equation 4.4, we find E_f = -2.4eV for stage 1. To determine f we may rewrite Equation 4.8 as

$$k_f = \sqrt{\pi n} = \sqrt{\frac{2\pi}{\Omega}}\, f/\ell \qquad 5.5$$

where Ω is the area of the $SbCl_5$ elementary unit cell, $\sim 36\text{Å}^2$, and f/ℓ is the number of holes per carbon atom. From the stoichiometry the charge transfer is given by $(f/\ell) \cdot 14$. This gives the unrealistic figure of f = 8; we would expect the acid molecule to be at most singly ionized.

We must note that from the model as described, it is not clear what criterion should be used for choosing which orbit is matched. If instead we choose to match the 11.4 MG orbit, we obtain $k_f = .19\text{Å}^{-1}$, E_f = -.99eV, and f = 3. However, this choice would predict only one orbit.

The same general procedure is used for predicting the FS of stages 2-4, except that the band structure relations are somewhat more

complex. Attempts at applying the stage 2 model were not satisfactory. For stage 2, two isoenergy surfaces, of radii k_{f1} and k_{f2} are adjusted to match our results. However, the choice of which observed orbits are matched again appears to be arbitrary in this model and leads to a variety of possible interpretations.[46] The band structure for both stages 3 and 4 are very complex and were not applied to our stage 4 compound.

We now turn to the dilute limit of this 2D model and apply it to the results obtained for our stage 6 and 8 compounds. According to this model, we should observe two Fermi surfaces, one due to pure graphite, the other due to a metallic sandwich consisting of the intercalant layer and its bounding graphite layers. The FS of the first component, graphite, is already known. The FS of the metallic sandwich is constructed as follows. From section 4.3.2 we again use the Harrison construction, but assume a nearly free electron (NFE) band structure. The Brillioun zone is again the one obtained from the $\sqrt{7} \times \sqrt{7}$ primitive cell and is shown in Figure 5.7. In that figure, we have shown the NFE isoenergy circle centered at the origin, and adjusted the radius, k_f, of this circle to match the largest observed frequency in the stage 6 compound, 6.5 MG. A single FS ellipse results along the zone edges. This requires that $k_f = .64\text{A}^{-1}$. From Equation 4.7 we determine f using $N = 1$ and $S_{BZ} = 1.085\text{A}^{-2}$. Again, the value obtained for f is greater than one ($f = 2.4$) which again is unrealistic for $SbCl_5$ compounds. We were unable to confirm the largest orbit in our stage 8 compound, and hence cannot apply this model. The second component for dilute compounds is pure 3D graphite. Thus, we expect to also observe the dHvA frequencies of graphite for compounds of stage index 4 and higher.

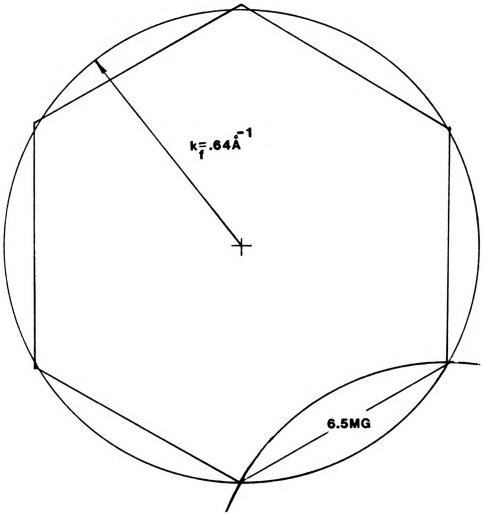

Figure 5.7 2D NFE FS Construction, Stage 6 $SbCl_5$.

Referring to Table 5.1, no graphite orbits are observed in either the stage 6 or stage 8 compounds.

The FS for the low stage compounds, n = 1-4, and for the metallic sandwich component of the dilute compounds, are cylindrical. Hence, we expect the dHvA frequencies for these cases to shift with angle according to Equation 5.2. This predicted angular dependence is shown in Figure 5.2, along with some of the rotation data obtained. As can be seen, data for all stages is consistent with either an ellipsoidal or a cylindrical FS model.

From this model it is difficult to obtain a single value of the Fermi energy which could be compared with the values in Table 5.5. The values that we obtain from our best fit to our observations imply Fermi energy shifts much larger than those listed in that table.

5.5 Conclusions

We evaluate the performance of these two Fermi surface models by, (1) comparing the predicted Fermi surface cross sections (dHvA frequencies) and their angular dependence with our experimental values, and by (2) comparing the resultant Fermi energy and its stage dependence from these models with the results of other types of experiments.

The rigid band model (RBM) gives qualitative agreement with the observed data for the appropriate range of stages studied, see Table 5.4. The 2D model and its dilute limit do not fare well for either the concentrated or dilute compounds. In regard to the geometrical information obtained to date, we cannot state whether the FS is elliptical (3D) or cylindrical (2D). Overall, however, the RBM appears to be superior in predicting the FS. We also recall here that this model has only one adjustable parameter, whereas in general the 2D models have several.

Probably the single most important parameter, and the one which is most directly measured both by Fermi surface techniques and by other experimental methods, is the Fermi energy, E_f. The values obtained from our experiment as interpreted by the rigid band model, and the values measured by optical studies, as well as those inferred from other data are listed in Table 5.5. The values from the RBM are in good agreement with those listed in that table. Values for E_f obtained from the 2D model are much larger. Again,the RBM appears to be superior to the 2D models.

In summary, we have made a systematic study of the stage dependence of the FS for carefully prepared and characterized $SbCl_5$ compounds. This study has included a wider range of stages than previous FS measurements for a single compound, extending from the most concentrated compound to well within the dilute limit. Our results are sample independent for samples of the same stage, and we observe a systematic decrease in the FS cross sections with increasing stage index. Results of previous dHvA FS studies on stages 2 and 4 are in general agreement with our results.

We have interpreted our data using two competing Fermi surface models. We find that the rigid band model best describes the observed FS and that parameters such as the Fermi energy as calculated from the RBM agree well with other experiments.

CONCLUSION

We have designed and used an experimental apparatus for detecting magnetothermal oscillations in high conductivity single crystals. A minicomputer has been interfaced to this apparatus, and is used for data acquisition and analysis. For high quality crystals this system provides accurate, high resolution Fermi surface (FS) data. Measurements can be performed on a variety of sample shapes, weights, and sizes.

This system has been employed to study the FS of $SbCl_5$ GIC's, stages 1-8. The compounds used in this research have been carefully characterized. The results obtained exhibit sample independence for samples of the same stage index. We have also found that with our system we are able to detect stage admixtures in the high stage compounds.

The results of our experiments have been analyzed using two competing theories proposed to describe the electronic structure (FS) of GIC's. We have found that one of these models, the rigid band model, is superior in predicting the observed FS results. Model dependent parameters, such as the charge transfer coefficient and the Fermi energy, calculated from our data as interpreted by this model, are in good agreement with measurements of these parameters by other techniques.

LIST OF REFERENCES

LIST OF REFERENCES

1. A.P. Cracknell and K.C. Wong, The Fermi Surface, Clarendon Press, Oxford (1973).

2. N.W. Ashcroft and N.D. Mermin, Solid State Physics, Holt, Rinehart, and Winston, (1976).

3. I.M. Lifshitz and A. Kosevitch, Sov. Phys. JETP 29, 730 (1955).

4. M.J. deHaas and P.M. van Alphen, Lieden Comm. 208(d), 212(a) (1930).

5. L. Onsager, Phil. Mag. 43, 1006 (1952).

6. R.B. Dingle, Proc. Roy. Soc. (London) A211, 517 (1952).

7. R.B. Dingle, Proc. Roy. Soc. (London) A211, 500, (1952).

8. J.C. Abele, Ph.D. dissertation, MSU Physics Department, (unpublished), (1968).

9. J.J. Higgins, Ph.D. dissertation, MSU Physics Department, (unpublished), (1977).

10. R.J. Higgins, Am. Journal of Phys. 44, 766 (1976).

11. S. Haykin, Communication Systems, J. Wiley and Sons (1978).

12. S.A. Solin, Adv. in Chem. Phys. 49, 455 (1982).

13. M.S. Dresselhaus and G. Dresselhaus, Adv. in Phys. 30, 139 (1981).

14. A. Herold, Bull. Soc. Chim. Fr., 999 (1955).

15. V. Murthy, D. Smith, P. Eklund, Mat. Sci. Eng. 45, 77 (1980).

16. J. Melin, A. Herold, C.R. Acad. Sci. Paris 269, 877 (1969).

17. R. Clarke, H. Homma, MRS Symposia Proceedings, Vol. 20, edited by M.S. Dresselhaus et al. (1982).

18. R. Clarke et al., Phys. Rev. B 26, 1 (1982).

19. M. Winokur, J. Rose, R. Clarke, Phys. Rev. B 25, 3703 (1982).

20. R. Clarke et al., Phys. Rev. Lett. 47, 1407 (1981).

21. L. Salamanca-Riba et al., MRS Symposia Proceedings, Vol. 20, edited by M.S. Dresselhaus et al. (1982).

22. P. Boolchand, W. Besser, D. McDaniel, and K. Sisson, Sol. State Comm. 40, 1049 (1981).

23. N. Bartlett, B. McQuillian, and A. Roberson, Mat. Res. Bull. 13, 1259 (1978).

24. F. Batallan, J. Bok, I. Rosenman, and J. Melin, Phys. Rev. Lett. 41, 330 (1978).

25. I.L. Spain, Chemistry and Physics of Carbon, Vol. 8 (1973).

26. J.C. Slonczewski and P.R. Weiss, Phys. Rev. 109, 272 (1958).

27. J.W. McClure, Phys. Rev. 104, 666 (1957).

28. J.W. McClure, Phys. Rev. 108, 612 (1960).

29. D.E. Soule, J.W. McClure, Smith, Phys. Rev. 134, A453 (1964).

30. S.J. Williamson, S. Foner, M. Dresselhaus, Phys. Rev. 140, A1429 (1965).

31. N.A.W. Holzwarth, S.G. Louie, S. Rabii, Phys. Rev. B 26, 5382 (1982).

32. M. Posternak et al., Phys. Rev. Lett. 50, 761 (1983).

33. P.R. Wallace, Phys. Rev. 71, 622 (1947).

34. G.S. Painter and D.E. Ellis, Phys. Rev. B 1, 4747 (1970).

35. J. Blinowski, C. Rigaux, et al., J. Physique 41, 47 (1980).

36. M.S. Dresselhaus, G. Dresselhaus, and J. Fischer, Phys. Rev. B 15, 3180 (1977).

37. M. Shayegan, M.S. Dresselhaus, and G. Dresselhaus, Phys. Rev. B 25, 4157 (1982).

38. H. Suematsu, S. Tanuma, and K. Higuchi, Physica 99B, 420 (1980).

39. G. Dresselhaus and S. Leung, Sol. State Comm. 35, 819 (1980).

40. G. Dresselhaus and S. Leung, Physica 105B, 495 (1981).

41. S. Leung and G. Dresselhaus, Phys. Rev. 24, 3490 (1981).

42. M. Shayegan and G. Dresselhaus, private communication.

43. I. Rosenman, F. Batallan, and G. Furdin, Phys. Rev. B 20, 2373 (1979).

44. W.A. Harrison, Pseudopotentials in the Theory of Metals, W.A. Benjamin, Inc., New York (1966).

45. J. Blinowski and C. Rigaux, J. Physique 41, 667 (1980).

46. C. Simon, F. Batallan, I. Rosenman, and H. Fuzeller, Phys. Rev. B 23, 2836 (1981).

47. D. Schoenberg, Phil. Trans. Roy. Soc. (London) A255, 85 (1962).

48. A.V. Gold, Solid State Physics, edited by J.F. Cochran and R.R. Haering, Vol. 1 (Gordon and Breach, New York, 1968), pp. 69-78.

49. L.M. Falicov and M.H. Cohen, Phys. Rev. Lett. 7, 231 (1961).

50. P. Schlottman and L.M. Falicov, Phys. Rev. Lett. 38, 855 (1977).

51. T.M. Rice and G.K. Scott, Phys. Rev. Lett. 35, 120 (1975).

52. Y. Iye, O. Takahashi, and S. Tanuma, Sol. State Comm. 33, 1071 (1980).

53. O. Takahashi, Y. Iye, and S. Tanuma, Sol. State Comm. 37, 863 (1981).

54. H. Fuzellier et al., Phys. Rev. B 23, 2836 (1981).

55. K. Higuchi, H. Suematsu, and S. Tanuma, J. Phys. Soc. Japan 48, 53 (1980).

56. P. Eklund et al., Syn. Metals 3, 111 (1981).

57. C.L. Foiles, private communication.

58. F. Batallan, I. Rosenman, and C. Simon, Syn. Metals 2, 353 (1980).

59. P. Eklund, 1983 APS March Meeting, private communication.